JOURNAL OF GEOPHYSICAL RESEARCH, VOL. 94, NO. C8, PAGES 10,937–10,954, AUGUST 15, 1989

An Ice-Ocean Coupled Model

GEORGE L. MELLOR AND LAKSHMI KANTHA[1]

Atmospheric and Oceanic Sciences Program, Princeton University, Princeton, New Jersey

An ice model, an ocean model, and a method of coupling the models are described. The ice model is a synthesis, with variations and extensions, of previous modeling ideas. Ice thickness, concentration, velocity, and internal energy are prognostic variables. The ice thermodynamics are represented by temperatures at the snow surface, ice surface, the interior, and the bottom surface. Melting and freezing rates are calculated at the ice-atmosphere, ice-ocean, and atmosphere-ocean interfaces. A prescribed portion of summer meltwater can be stored on the surface and refrozen in the fall. The ocean model includes a second moment, turbulence closure submodel and enables one to solve for oceanic heat flux, the interfacial stress, and subsurface properties. In this paper the model is applied to one-dimensional simulations, but the equations are cited in a form for implementation by two- and three-dimensional models. In a companion paper (Kantha and Mellor, this issue) the model is used for two-dimensional (vertical plane) simulations in the Bering Sea. Several one-dimensional sensitivity studies are performed in the case where the ice model is decoupled from the ocean; here the oceanic heat flux and sea surface temperature are prescribed constants. The studies reveal the role and sensitivity of surface trapped meltwater, ice concentration, and ice divergence. With the coupled ice-ocean model, the seasonally varying oceanic heat flux and mixed layer properties are determined by the model. Some comparisons with observations in the central Arctic ocean are possible. The role of the molecular sublayer immediately adjacent to the ice is examined; frazil ice production is related to the large disparity in the molecular diffusivities for temperature and salinity. The mixed layer model contains empirical constants which are known from turbulence data. The molecular sublayer parameterization requires one empirical parameter b, which is uncertain but, from this study, is assuredly greater than zero, the value implicit in previous models. The ice model requires the empirical parameters Φ_F and Φ_M to quantitatively account for freezing or melting processes in open leads; their values are also uncertain, but we present reasoning and sensitivity studies to suggest specific values. Finally, an empirical parameter G is introduced; it is the ratio of the value of the ice thickness used to represent average ice volume in the dynamic and thermodynamic equations to the value of the thickness needed in the heat conduction equation. Estimates of G are made from observed thickness distribution functions; sensitivity studies show it to be an important parameter.

1. INTRODUCTION

There has been evolutionary progress toward completely coupled, ice-ocean, numerical models. At first, decoupled models were the general rule. *Semtner* [1976*b*] performed an ocean modeling study of the Arctic basin wherein ice properties were prescribed, and the general circulation was calculated by his model. On the other hand, there have been many more modeling studies where ice is explicitly modeled and where oceanic parameters were prescribed. *Maykut and Untersteiner* [1971] (hereinafter MU) developed a one-dimensional thermodynamic ice model which was simplified and shown by *Semtner* [1976*a*] to perform well even if the ice is represented by a low-resolution vertical grid. *Parkinson and Washington* [1979] used Semtner's model and a simplified ice dynamics model to simulate the yearly ice cycle in the Arctic and Antarctic. *Hibler* [1979] developed a horizontally two-dimensional, transport model of the Arctic basin which exhibited realistic properties; he used ice growth rates which were prescribed a priori as a function of ice thickness and time of the year; such a formulation is, of course, limited to specific geography and excludes processes such as oceanic feedback.

Recently, the papers by *Hibler and Bryan* [1987] and *Semtner* [1987] brought forth simulation studies of the Arctic basin using coupled ice-ocean models. It is apparent from these papers that the oceanic heat flux distribution does play an important role in determining the location of the marginal ice zone and the other ice cover properties such as mean ice thickness and concentration. However, these models did not incorporate mixed layer physics even though the mixed layer ought to be considered the essential coupling medium for a coupled model. A one-dimensional mixed layer model has very recently been developed by *Lemke* [1987] and coupled to Semtner's ice model. His mixed layer model is considerably more empirical than that used here. The model is a purely thermodynamic model; dynamic oceanic feedback is excluded.

One early goal of this paper was to match the turbulence closure model of *Mellor and Yamada* [1982] which has already been imbedded in a ocean model [*Blumberg and Mellor*, 1983, 1987; *Oey et al.*, 1985*a*, *b*, *c*], to an ice model. For the ice portion the starting point was the one-dimensional model of MU and the finding by *Semtner* [1976*a*, *b*] that a low-resolution model should provide sufficient accuracy to represent internal and surface ice temperatures. However, we have added the effect of the concentration variable A, which is an ensemble-averaged fraction of ice-covered ocean area. This variable is included in the two-dimensional model of *Hibler* [1979] and the subsequent models of *Hibler and Bryan* [1987] and *Semtner* [1987]; there the model equation for A differs qualitatively from the present version and differs quantitatively in at least one important aspect concerning shortwave radiation absorption in open leads. The present model is not specific to geography

[1]Now at Institute of Naval Oceanography, Stennis Space Center, Mississippi.

Paper number 89JC00158.
0148-0227/89/89JC-00158$05.00

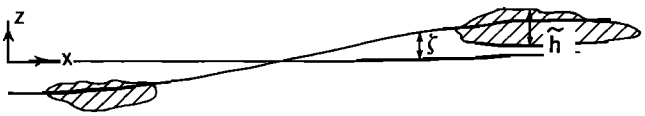

Fig. 1. The sea surface elevation ζ and the local floe thickness $\tilde{h}$.

or climatology since ice growth is related to local atmospheric and oceanic forcing. Finally, the means of matching the ice model dynamically and thermodynamically to the ocean model, provided by *Mellor et al.*, [1986] and *Steele et al.*, [1989] are incorporated here.

The model is meant to be applied in a three-dimensional context. However, in this paper, sensitivity studies with forcing appropriate to the central Arctic are executed in a one-dimensional mode. We wish to learn as much about the model as possible before proceeding to three dimensions, where it is considerably more difficult to explore parameter space. In particular, we will determine how the model behaves when subject to a diverging ice field, since divergence is an important component of the overall ice budget. Other parameter sensitivities are studied as is the overall impact of oceanic feedback.

2. The Ice Model

We describe an ice model which is similar to the lowest-resolution ice model of *Semtner* [1976*a*]; however, here we build in the effect of the concentration variable A, which is a statistical quantity denoting the fractional area covered by ice, whereas $(1 - A)$ is the fractional open water so that $0 \leq A \leq 1$. We define the sea surface elevation ζ and the local ice floe thickness $\tilde{h}$ according to Figure 1. The variable h_I will be the average ice thickness, where the average is taken only over ice covered areas. Thus Ah_I is the average thickness over the total area. This is a relatively simplistic description of an ice field, compared to studies by *Thorndike et al.* [1975], *Hibler* [1980], and *Maykut* [1982], wherein one attempts to model a thickness distribution function $g(\tilde{h})$. Instead, we deal only with the concentration A and the moment

$$h_I = \int_0^\infty \tilde{h} g(\tilde{h})\, d\tilde{h} \tag{1}$$

The Momentum Equation

At a given horizontal point the ice velocity is characterized by a velocity vector $U_{Ii}(i = x, y)$. The dynamic equation applicable to open water ($A = 0$), an ensemble of ice floes ($A < 1$), or for solid ice ($A = 1$) is

$$\frac{\partial}{\partial t}(Ah_I U_{Ii}) + \frac{\partial}{\partial x_j}(Ah_I U_{Ij} U_{Ii}) - Ah_I \varepsilon_{ijk} f_j U_{Ik}$$

$$= Ah_I g \frac{\partial \zeta}{\partial x_i} + \frac{1}{\rho_I}\frac{\partial \sigma_{ij}}{\partial x_j} + \frac{A}{\rho_I}(\tau_{AIi} - \tau_{IOi}) \tag{2}$$

where $f_j = (0, 0, f)$ and f is the Coriolis parameter; ρ_I is the density of ice; σ_{ij} is the internal ice stress tensor; τ_{AIi} is the atmospheric wind stress; τ_{IOi} is the ice-ocean interfacial stress; and g is the gravity constant. τ_{AIi} is calculated according to bulk drag relations, which are collected in Appendix A. The ice-ocean interface stress τ_{IOi} is obtained from a bulk drag relation in the stand-alone ice model but is calculated according to the mixed layer physics described in section 3 in the coupled ice-ocean model.

The internal stresses σ_{ij} are not required in the one-dimensional calculations exercised in this paper. Their consideration will therefore be postponed to a companion paper [*Kantha and Mellor*, this issue] where they are needed in two-dimensional calculations.

The Equations for Mass and Concentration

The equation for the conservation of the mass of ice is

$$\frac{\partial}{\partial t}(Ah_I) + \frac{\partial}{\partial x_i}(Ah_I U_{Ii})$$

$$= \frac{\rho_o}{\rho_I}[A(W_{IO} - W_{AI}) + (1 - A)W_{AO} + W_{FR}] \tag{3}$$

The various volumetric fluxes are illustrated in Figure 2; they are all positive upward and correspond to melting or freezing, depending on their location. Thus W_{AI} is melt rate (positive) on the top of the ice; W_{AI} is also a freeze rate (negative) when trapped surface water refreezes in late summer. W_{IO} is the freeze rate (positive) of congelate ice at the ice-ocean interface. W_{AO} is the melt (negative) or freeze rate (positive) in open water, a problematic term which will be discussed shortly. W_{FR} is the rate of ice accretion at the surface due to frazil ice growth in the water column. This will also be discussed in detail later on.

The equation for ice concentration A is

$$h_I\left[\frac{\partial A}{\partial t} + \frac{\partial}{\partial x_i}(AU_{Ii})\right]$$

$$= \frac{\rho_o}{\rho_I}[\Phi\,(1 - A)W_{AO} + (1 - A)W_{FR}] \qquad 0 \leq A \leq 1 \tag{4}$$

Equation (3) is an exact conservation equation, whereas (4) is an empirical equation first introduced by *Nikiferov* [1957], although he omitted melting and freezing terms. A version of (3) and (4) wherein net ice growth rate was prescribed a priori has been described by *Hibler* [1979]; we will comment on Hibler's model later.

We next discuss certain properties of these equations. First, consider their purely dynamical properties, where we temporarily neglect the right sides of (3) and (4); that is, we neglect thermodynamic forcing. Equation (3) is an exact equation. On the other hand, equation (4) is such a simple-looking equation that it is necessary to keep in mind that it is empirical and is intimately associated with the (idealized)

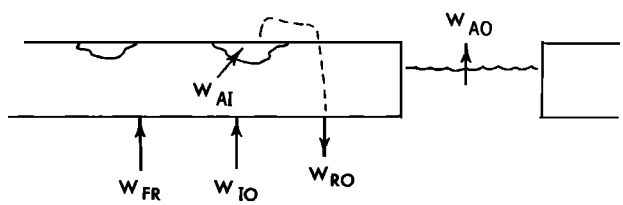

Fig. 2. A sketch of water to ice, volume flux, or vice versa, across the ice-ocean interface W_{IO}, the ice-atmosphere interface W_{AI}, and the atmosphere-ocean interface W_{AO}. The W_{AI} flux can be trapped and, subsequently, run off into the ocean as W_{RO} or can be refrozen. W_{FR} is the frazil ice flux.

constitutive properties of ice wherein one assumes that ice cannot be horizontally dilated without creating open water. Thus write (4) as $DA/Dt = -A\,\partial U_{Ii}/\partial x_i$. Now the divergence $\partial U_{Ii}/\partial x_i$ is the rate of creation of new area following a Lagrangian or material surface. In Figure 3 we sketch a material surface where $A = 1$ at $t = 0$. After a small interval of time Δt, equation (4), for positive divergence, yields a decrease in A according to $\Delta A = -(\partial U_{Ii}/\partial x_i)\,\Delta t$. Furthermore, according to a combination of (3) and (4), $Dh_I/Dt = 0$. Therefore open water is formed, but the average thickness of the ice is unchanged. On the other hand, if the divergence is negative, the constraint, $A \leq 1$, overrides the differential equation, and $A = 1$ at $t = \Delta t$. Equation (3) now yields an increase in h_I according to $Dh_I/Dt = -h_I(\partial U_{Ii}/\partial x_i)$. This simulates ridging. Thus equation (4) is a deceptively simple but, nevertheless, remarkable relation.

Now reinstate the right side of equation (3), which contains source (freezing) or sink (melting) terms which are relatively straightforward. Also, reinstate the right side of (4), where the terms are not straightforward. In particular, the atmospheric ocean melt rate W_{AO} requires explanation, as does the empirical factor Φ in equation (4). As discussed in section 3, we assume, so long as $A > 0$, that the sea surface temperature is at the freezing temperature corresponding to the surface salinity and is horizontally homogeneous. Then the energy gain or loss rate to open leads is instantaneously converted to a melt or freeze rate W_{AO}. We must decide what to do with this positive or negative energy rate under the simplifying terms of the present model. Toward this end we distinguish between freezing and melting such that

$$\begin{aligned} &\text{Freezing} \quad \Phi = \Phi_F \qquad W_{AO} > 0 \\ &\text{Melting} \quad \Phi = \Phi_M \qquad W_{AO} < 0 \end{aligned} \tag{5}$$

Consider the case where $W_{AI} = W_{FR} = 0$. Now subtract (4) from (3) to obtain $A[\partial h_I/\partial t + U_{Ii}\partial(h_I)/\partial x_i] = (\rho_o/\rho_I)[AW_{IO} + (1 - \Phi)(1 - A)\,W_{AO})]$. Thus positive (negative) W_{IO} increases (decreases) the thickness of the ice without changing the ice-covered area, since the term is absent in (4); this behavior is, of course, correct, since W_{IO} was defined as the freezing or melting rate at the base of the ice. Now consider the term involving W_{AO} and its coefficient $(1 - \Phi)$. If we were to set $\Phi = 1$, W_{AO} would not effect h_I but would change A; the interpretation is that ice would be melted or frozen only at the edge of leads. On the other hand, if $\Phi > 1$, W_{AO} contributes to the freezing or melting of open water. The latter process is, of course, impossible, but in the freezing case we do expect open water to form ice cover and therefore we expect that $\Phi_F > 1$ when $W_{AO} > 0$.

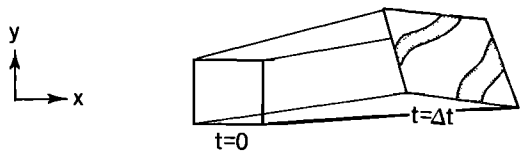

Fig. 3. The creation of open water according to equation (3). In this illustrative example, at $t = 0$, $A = 1$ the material area is completely ice covered. At $t = \Delta t$ the material area increases by the fraction $\nabla \cdot \mathbf{U}_I\,\Delta t$, so that the fractional ice coverage A decreases according to $\Delta A \simeq -\nabla \cdot \mathbf{U}_I\,\Delta t$.

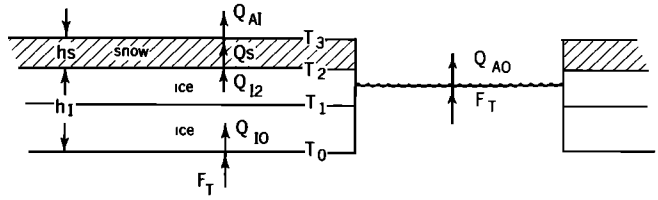

Fig. 4. A sketch of the internal ice temperatures and the heat fluxes through the ice.

For the melting case some of the melting can take place at the ice edge, but some of the excess heat represented by $W_{AO} < 0$ can also be transported under the ice and therefore should decrease h_I. In fact, $W_{AO} < 0$ is mostly determined by summertime, shortwave radiation which can penetrate well into the mixed layer; the analysis by *Maykut and Perovich* [1987] suggests a value like $\Phi_M = 0.5$.

We should mention here that it is a fairly simple matter to allow shortwave penetration into the ocean surface in our model [*Simpson and Dickey*, 1981; *Martin*, 1985]. This would decrease heat absorbed at the surface and decrease W_{AO}, thereby alleviating some of the empiricism associated with that variable. The penetrating radiation would be absorbed in the ocean and then reappear as uniformly distributed surface heat flux. However, in the interest of consistency, we will not invoke the penetration process in this paper since it cannot be invoked when we decouple the ice model from the ocean model.

It is anticipated that more sophisticated models for Φ will be developed in the future on the basis of more detailed analyses such as those by *Bauer and Martin* [1983], where one learns that ice edge accumulation is wind dependent, and *Maykut and Perovich* [1987], which contains a short review of the problem and a relatively detailed analysis. In this paper we will later perform calculations to determine the sensitivity of Φ_F and Φ_M to ice development in the central Arctic and then, finally, select the values $\Phi_F = 4$ and $\Phi_M = 0.5$.

The formulation in (4) makes its empirical nature more transparent than the analogous formulation by *Hibler* [1979], and for this reason we prefer it. However, a comparison of the two formulations reveals that Hibler's equation for the freezing case may be recovered if we set $\Phi_F = h_I/h_0$ where, empirically, $h_0 = 0.5$ m. For thick ice we expect a behavior similar to our model but, for thin ice, open water would not freeze at all, since $\Phi_F < 1$. For the melting case, Hibler included a contribution due to W_{IO} (using the present nomenclature) in his equation corresponding to (4). However, if we ignore the W_{IO} contribution in Hibler's equation and the W_{FR} contribution in (4), his equation would correspond to (4), where $\Phi_M = 0.5$. This is an apparent coincidence, since he arrives at that number on entirely different physical reasoning than used here. Hibler's model for summertime melt rate does not include the large amount of shortwave radiation captured by open leads because of the greatly reduced albedo of open ocean compared to ice cover. In our case this effect is important in the summer when $A < 1$.

The Thermodynamic Ice Equations

The thermodynamic model is sketched in Figure 4. The numerical scheme will use three layers; the top layer is a

TABLE 1. Physical Constants

Parameter	Value
Reference water density	$\rho_o = 1026$ kg m^{-3}
Reference air density	$\rho_a = 1.27$ kg m^{-3}
Reference ice density	$\rho_I = 900$ kg m^{-3}
Thermal ice conductivity*	$k_I = k_{oI}(1 - 1.2\,r)$; k_{oI} = 2.04 J m^{-1} s^{-1} K^{-1}
Thermal snow conductivity	$k_s = 0.31$ J m^{-1} s^{-1} K^{-1}
Specific heat of seawater	$C_{po} = 3990$ J kg^{-1} K^{-1}
Specific heat of air	$C_{pa} = 1005$ J kg^{-1} K^{-1}
Specific heat of ice	$C_{pI} = 2093$ J kg^{-1} K^{-1}
Seawater kinematic viscosity	$\nu = 1.8\ 10^{-6}$ m^2 s^{-1}
Seawater salinity diffusivity	$\alpha_t = 6.8\ 10^{-10}$ m^2 s^{-1}
Seawater heat diffusivity	$\alpha_s = 1.39\ 10^{-7}$ m^2 s^{-1}
Stefan Boltzmann constant†	$\sigma = 5.67\ 10^{-8}$ W m^{-2} K^{-4}
Albedo of open ocean surface	$\alpha_o = 0.1$
Albedo of ice or snow	see equation (36)
Emissivity of ocean surface‡	$\varepsilon_o = 0.97$
Emissivity of ice surface	$\varepsilon_I = 0.97$
Emissivity of snow surface	$\varepsilon_s = 0.97$
Latent heat of fusion	$L_F = 3.347\ 10^5$ J kg^{-1}
Latent heat of sublimation	$L_s = 2.834\ 10^6$ J kg^{-1}
Latent heat of evaporation	$L_v = 2.501\ 10^6$ J kg^{-1}
Constants in (32)	$m = 0.0543$ K/ppt $n = -0.000759$ K m^{-1}
Ice roughness parameter	$z_{0I} = 0.05\ h_I/3$

*Originally we had supposed that $k_I = k_{oI}(1-r) + k_b r$ where k_b is the conductivity of brine, $k_b/k_{oI} \simeq 0.28$, and r is the brine fraction. However, the version cited in the table is more nearly in accord with *Untersteiner* [1961].

†For most of the calculations in this paper we use the value 5.78 $\times$ 10^{-6} W m^{-2} K^{-4}, as explained in the text.

‡However, for comparison with the MU calculations, we have set $\varepsilon_o = \varepsilon_I = \varepsilon_s = 1.0$.

snow layer whose roles are as an insulator and as an absorber of incoming radiation as it melts in the spring; the sensible heat capacity of the snow is neglected.

An equation of state for both ice and seawater will be required; a good approximation is

$$E(T, r) = r(L_F + C_{po}T) + (1 - r)\,C_{pI}T \tag{6}$$

where r is the brine fraction; thus $E(T, 0) = C_{pI}T$ is the enthalpy of pure ice, whereas $E(T, 1) = L_F + C_{po}T$ is the enthalpy of seawater. L_F is the latent heat of fusion. Physical constants are listed in Table 1.

Since this is meant to be a low-vertical-resolution model, we set the average salinity of the ice as vertically constant and label it S_I. The salt content is contained in brine pockets wherein, locally, the salinity is T_1/m. The ice temperature is evaluated at T_1, and m is the slope of the freezing line; therefore the brine fraction is $r_1 = S_I\,m/T_1$. For nonzero S_I the specific heat capacity $\partial E/\partial T$, as obtained from (6), is a function of T_1 and S_I, and this, coupled with the dependence of ice conductivity (see Table 1) on brine fraction, renders the results dependent on S_I.

The net heat flux Q_{AI} between atmosphere and snow or ice is given by

$$Q_{AI} = Q_{SI} + Q_{LI} - (1 - \alpha_I)SW - LW + \varepsilon_I\sigma(T_3 + 273)^4 \tag{7}$$

where Q_{SI} is the sensible heat transfer and Q_{LI} is the latent heat transfer. SW and LW are the incoming shortwave and longwave radiation, respectively; α_I is the ice or snow albedo, the fraction of shortwave radiation reflected back into the atmosphere. The outgoing longwave, radiative emmission from the surface of the ice is $\varepsilon_I\sigma(T_3 + 273)^4$. The coefficient σ is the Stefan-Boltzman constant, and ε_I is the emissivity.

The equation for the direct transfer of atmospheric heat flux to the ocean through open ocean or leads is

$$Q_{AO} = Q_{SO} + Q_{LO} - (1 - \alpha_o)SW - \varepsilon_o LW + \varepsilon_o\sigma(T_0 + 273)^4 \tag{8}$$

where Q_{SO} is the sensible heat transfer and Q_{LO} is the latent heat transfer. α_o and ε_o are the albedo and emissivity of open water. Formulas for the atmospheric flux components in (7) and (8) are given in Appendix A.

Since the model snow does not have heat capacity, the heat conduction through the snow is given by

$$Q_s = \frac{k_s}{h_s}(T_2 - T_3) \tag{9a}$$

where h_s is the thickness of the snow and k_s is the heat conductivity of snow. The heat conduction at the top of the ice layer is

$$Q_{I2} = \frac{k_I}{h_I/2}(T_1 - T_2) \tag{9b}$$

where h_I is the thickness of the ice and k_I is the heat conductivity. Since we neglect heat capacity in the snow layer, $Q_s = Q_{I2}$. Together with (9a) and (9b), we use this equality to obtain a relation between T_3, T_2, T_1, and T_0 (which, of course, yields $T_2 = T_3$ when $h_s = 0$); then T_2 is eliminated from (9a).

We next consider the relation between Q_{AI} and Q_{I2}. When T_3 is below the freezing point, Q_{AI} and Q_{I2} are equated to obtain T_3 (see Appendix B); otherwise, T_3 equals the freezing temperature (273 K), and the resulting inbalance between Q_{AI} and Q_{I2} causes snow to melt or, if $h_s = 0$, then the ice melts. In the latter case the melt rate at the top, W_{AI}, is obtained from an energy balance across an infinitesimally thin control volume which includes the atmosphere-ice interface. Thus

$$W_{AI} = (Q_{AI} - Q_{I2})/(\rho_o L_3) \tag{10a}$$

$$L_3 \equiv [E(T_3,1) - E(T_1, r_1)] \tag{10b}$$

Note that $L_3 = (1 - r_1)L_F$ plus a small sensible heat correction.

At the bottom of the ice the heat conduction is

$$Q_{IO} = \frac{k_I}{h_I/2}(T_0 - T_1) \tag{11}$$

The relationship between Q_{I2} and Q_{IO} involves the heat capacity of the ice such that

$$\rho_I h_I\left[\frac{\partial}{\partial t}E(T_1, r_1) + U_{Ii}\frac{\partial}{\partial x_i}E(T_1, r_1)\right] = Q_{IO} - Q_{I2} \tag{12}$$

It should be noted that (12) would be exact if E were taken as the vertically averaged internal energy of the ice; it is an approximation, albeit a minor approximation, to evaluate E at T_1, the temperature at the middle of the ice layer.

Surface Water Accumulation

Water due to melted snow or ice can be stored on the surface, thus simulating standing pools of water; the maxi-

mum depth of stored water will be denoted by h_{sw}. Excess meltwater runoff, denoted as W_{RO}, is combined with the bottom freeze or melt rate W_{IO} and enters the ocean surface layer. Note that if $h_{SW} = 0$, then $W_{RO} = W_{AI}$. There is further discussion of this feature in section 5.

3. Surface Boundary Conditions for the Ocean

In the paper by *Mellor et al.* [1986] the ice velocity or the ice-ocean stress was prescribed as an external parameter in order to focus on thermodynamic boundary conditions and the melting or freezing process. Here we repeat some of that material, with the additional complexity of the concentration variable A.

The boundary condition for stress is

$$K_M\left(\frac{\partial U}{\partial z}, \frac{\partial V}{\partial z}\right) = \frac{A}{\rho_o}(\tau_{IOx}, \tau_{IOy}) + \frac{(1-A)}{\rho_o}(\tau_{AOx}, \tau_{AOy}) \qquad z \to 0 \tag{13}$$

where (τ_{IOx}, τ_{IOy}) is the ice-ocean interfacial stress given by

$$\frac{1}{\rho_o}(\tau_{IOx}, \tau_{IOy}) = \frac{ku_\tau}{\ln(z/z_0)}(U_I - U, V_I - V) \qquad z \to 0 \tag{14}$$

The mixing coefficient K_M will be discussed later. The friction velocity is $u_\tau \equiv (\tau_{IO_x}^2 + \tau_{IO_y}^2)^{1/4}\rho_o^{-1/2}$. The von Karman's constant is $k = 0.4$, and z_0 is the roughness parameter. (τ_{AOx}, τ_{AOy}) is the wind stress applied directly to open water. The combination of (13) and (14) is a mixed Neuman-Dirichlet boundary condition for velocity (U, V) which, numerically, is applied to the first grid point nearest the surface layer of the ocean model described in section 4. The ice velocity (U_I, V_I) is obtained from (2).

Recall that the freezing rates (positive value) or melting rates (negative value) are denoted by W_{IO} for ice covered water and W_{AO} for open water, as illustrated in Figure 2. The energy balance across an infinitesimally thin control volume which, first, includes the ice-ocean interface and, second, the atmosphere-ocean interface are

$$F_T = Q_{IO} - W_{IO}\rho_o L_o \tag{15a}$$

$$F_T = Q_{AO} - W_{AO}\rho_o L_o \tag{15b}$$

where

$$L_o \equiv [E(T_0, 1) - E(T_1, r_1)] \tag{15c}$$

The product of density and melt or freeze rate is continuous across the interface. In this paper, melt or freeze rates are consistantly referred to the water side so that the product of seawater density and melt rate is the melt mass rate. Equations (15*a*) and (15*b*) may be conveniently combined such that

$$F_T = (AQ_{IO} + (1-A)Q_{AO}) - W_O L_o \tag{16a}$$

$$W_O \equiv AW_{IO} + (1-A)W_{AO} \tag{16b}$$

Then the heat flux boundary condition is

$$F_T/(\rho_o C_{po}) = -C_{Tz}(T_0 - T) \qquad z \to 0 \tag{17}$$

where we define

$$C_{Tz} = \frac{u_\tau}{(P_{rt}\,k^{-1}\ln(-z/z_0) + B_T)} \tag{18a}$$

$$B_T = b\left(\frac{z_0 u_\tau}{\nu}\right)^{1/2} Pr^{2/3} \tag{18b}$$

This formulation is similar to that of *Mellor et al.* [1986]. However, as discussed by *McPhee et al.* [1987] and *Steele et al.* [1989], we are now more appreciative of the importance of the molecular sublayer correction of (18*a*) and (18*b*), contained in the factor B_T, which has been researched by *Owen and Thompson* [1963] and others using data from laboratory flows over rough surfaces. Equation (18*b*) is a more recent but similar formula obtained by *Yaglom and Kader* [1974]. Here Pr is the molecular Prandtl number, which we take to be 12.9, and the turbulent Prandtl number P_{rt} is 0.85. The factor b in equation (18*b*) has been determined to be 3.14 by Yaglom and Kader. The actual equation is

$$B_T = b(z_0 u_\tau/\nu)^{1/2}(Pr^{2/3} - 0.2) + 2.3$$

However, the additional constants are unimportant in the present context. Also, we have simplified their symbol, B_T^{-1}, to the present B_T. Although the above forms are convenient analytically and numerically, another form has more physical appeal. Thus combine (17), (18*a*), and (18*b*) so that $(T - T_0) = F_T/(\rho_o C_p)[P_{rt}(ku_\tau)^{-1}\ln(-z/z_0) + \delta_t/\alpha_t]$. The first and second terms represent the temperature changes across the turbulent and molecular portions of layer, respectively. The effective thickness of the molecular sublayer is given by $\delta_t = b\,z_0(\alpha_t/u_\tau\,z_0)^{1/2}(\alpha_t/\nu)^{1/6}$. This scaling is appropriate to an embedded, steady laminar layer [*Schlichting*, 1978].

A value of b appropriate to ice-ocean interaction will later be the subject of discussion and analysis. For $b > 1$, B_T is considerably larger than the logarithmic term in (18*a*).

Note that we take the ocean immediately below the surface to be horizontally homogeneous so that the left sides of (15*a*) and (15*b*) are equal to the oceanic heat flux F_T, which is related to the near subsurface properties of the ocean according to equation (17). Also, note that, in principle, z_0 or C_{Tz} and, accordingly, T_0 could be different at the surfaces of open and ice-covered water even though F_T and T are not. However, at present we will bypass this complexity and assume that they are the same. However, we determine z_o according to

$$\ln z_0 = A\ln z_{0I} + (1-A)\ln z_{0O} \tag{19}$$

which *Taylor* [1987] argues is the best way to average two regions with different roughness parameters. Here z_{0I} is a best guess of the ice roughness parameter. For the calculations of this paper we have chosen a value of 0.05 m when $h_I = 3$ m and have linearly decreased z_0 to zero when h_I is zero. For the ocean roughness parameter we use Charnock's wave roughness relation, $z_{0O} = 0.016\,(\rho_o/\rho_a)u_\tau^2/g$; it is assumed that the waterside roughness equals the airside roughness.

The salt balance across the ocean interface is

$$F_S = (W_O - AW_{RO})(S_I - S_0) + (1-A)S_0(\dot{P} - \dot{E}) \tag{20}$$

where $\dot{P} - \dot{E}$ represents the volume surface flux due to precipitation and evaporation, and W_{RO} is the runoff from surface melting.

The corresponding salt flux equations are

$$F_S = -C_{Sz}(S_0 - S) \qquad z \to 0 \tag{21}$$

where

$$C_{Sz} = \frac{u_\tau}{(P_{rt}k^{-1}\ln(-z/z_0) + B_S)} \tag{22a}$$

$$B_S = b\left(\frac{z_0 u_\tau}{\nu}\right)^{1/2} Sc^{2/3} \tag{22b}$$

The above formulae are identical to (18*a*) and (18*b*) except that Pr is replaced by the Schmidt number, $Sc \equiv \nu/\alpha_s = 2432$, for salt diffusion.

The above equations are subject to the constraints

$$W_O = 0 \qquad A = 0 \tag{23a}$$

or

$$T_0 = mS_0 \qquad A > 0 \tag{23b}$$

The later equation states that, if ice is present, the ocean surface properties are on the freezing transition interface. We let m be constant, as listed in Table 1.

Numerically, T and S at z, the first grid point nearest the oceanic surface, is obtained from the oceanic solution at the previous time level; C_{Tz} and C_{Sz} are also known. Then (16*a*), (17), (20), (23*a*), and (23*b*) can be solved for W_O, T_0, S_0, F_T, and F_S (see Appendix B).

The temperature and salinity boundary conditions applied to the ocean are $F_T = -K_H\,\partial T/\partial z$ and $F_S = -K_H\partial S/\partial z$ as $z \to 0$. However, we find it numerically more robust to use (17) and (21) so that

$$-K_H\frac{\partial T}{\partial z} = C_{Tz}(T_0 - T) \qquad z \to 0 \tag{24}$$

$$-K_H\frac{\partial S}{\partial z} = C_{Sz}(S_0 - S) \qquad z \to 0 \tag{25}$$

which are mixed Neuman-Dirichlet surface boundary conditions for $T(z)$ and $S(z)$.

4. The Ocean Model

The Three-Dimensional Ocean Model

Although, in the present paper, we cite only one-dimensional calculations, we include here a description of the three-dimensional model we use in order to set the stage for future two- and three-dimensional simulations. In a companion paper [*Kantha and Mellor*, this issue] the model is applied to two-dimensional simulations of the Bering Sea. The ocean model we use has been previously described in the literature [*Blumberg and Mellor*, 1983; *Oey et al*, 1985*a*, *b*, *c*; *Blumberg and Mellor*, 1987]. We briefly note here that it is a sigma coordinate model; it has a free surface and a split mode time step and an imbedded turbulence closure submodel. It solves the following equations for the ocean velocity (U, V), potential temperature T, and salinity S:

$$\frac{\partial U_i}{\partial x_i} = 0 \tag{26}$$

$$\frac{\partial}{\partial t}(U, V) + \frac{\partial}{\partial x_i}[U_i(U, V)] + f(-V, U) = -\frac{1}{\rho_o}\left(\frac{\partial p}{\partial x}, \frac{\partial p}{\partial y}\right) + \frac{\partial}{\partial z}\left[K_M\frac{\partial}{\partial z}(U, V)\right] \tag{27}$$

$$\frac{\partial T}{\partial t} + \frac{\partial}{\partial x_i}(U_i T) = \frac{\partial}{\partial z}\left[(K_H + \alpha_t)\frac{\partial T}{\partial z}\right] \tag{28}$$

$$\frac{\partial S}{\partial t} + \frac{\partial}{\partial x_i}(U_i S) = \frac{\partial}{\partial z}\left[(K_H + \alpha_s)\frac{\partial S}{\partial z}\right] \tag{29}$$

The hydrostatic approximation yields

$$\frac{p}{\rho_o} = g\zeta + \int_z^0 \frac{\rho(z')}{\rho_o}\,g\,dz' \tag{30}$$

where $\rho = \rho(T, S, p)$. The equations, after transformation to a sigma coordinate system, can be found in the papers cited above.

The Turbulence Closure Model

To obtain the vertical mixing coefficients K_M and K_H, the turbulence closure model of *Mellor and Yamada* [1974, 1982] is embedded in the numerical model; we use the so-called level 2 1/2 version of the closure model. Although one must refer to the cited papers for a complete account of model derivation, we provide brief commentary here.

The closure model begins with the prognostic equations for all six components of the Reynolds stress tensor and three components of the heat and salinity (when applied to the ocean) flux vectors. Closure hypotheses for the pressure-velocity gradient correlation tensor, following *Rotta* [1951*a*, *b*], and the dissipation tensor, following *Kolmogorov* [1941], are adopted and extended to similar terms involving density fluctuations. Terms for all stress and flux components and for shear and buoyancy production appear quite naturally and do not require modeling. Turbulent diffusion terms are also modeled but are not of primary importance. Nondimensional model constants are determined from neutral laboratory data. An early application of the model [*Mellor*, 1973] yielded Monin-Obkhov similarity relations in close agreement with near-surface, atmospheric boundary layer data.

The complete model calling for the solutions of prognostic equations for all stress and flux components was labeled the level 4 model. *Mellor and Yamada* [1974] then developed a procedure to approximate the full prognostic equation set in order to reduce their number and reduce complexity and computational cost. As summarized by *Mellor and Yamada* [1982], there now exist level 1, 2, 3, and 4 models, and somewhat as an afterthought, a level 2½ model was defined and is used here. This requires prognostic equations for q^2, twice the turbulence kinetic energy, and q^2l where l is a turbulence macroscale; it is approximately proportional to the integral of the velocity correlation function and is deliberately scaled so that, adjacent to a surface, it is asymptotically equal to Prandtl's mixing length as the surface is approached. These prognostic equations are similar in form to (28) or (29) except that turbulence production and dissipation terms are included. Vertical mixing coefficients for velocity and temperature (or any scalar) are provided by the relation $(K_M, K_H) = lq\,(S_M, S_H)$. S_M and S_H are stability coefficients and are functions of $l^2[\partial U/\partial z)^2 + (\partial V/\partial z)^2]/q^2$ and

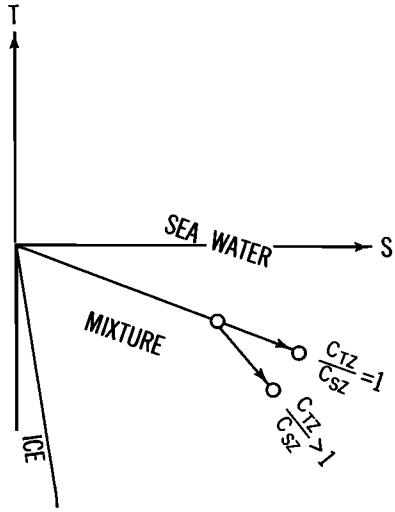

Fig. 5. Equilibrium phase diagram for ice-seawater, delineating regions of seawater, seawater-ice mixture, and ice. The areal extent of the latter region is exaggerated; ice crystal structure accomodates only negligibly small concentrations of salt. The arrows represent changes, starting from states on the freezing line. As explained in the text, the condition $C_{Tz} > C_{Sz}$ results in frazil ice production.

$l^2 g\rho_o^{-1}[\partial\rho/\partial z]/q^2$. Here ρ is density, defined by an equation of state $\rho(T, S)$, and ρ_o is a reference density. It is assumed that the Reynolds and Peclet numbers are very large; a result is that K_H is also the vertical mixing coefficient for salinity and, in fact, for any other scalar property.

Frazil Ice

Because $C_{Tz} > C_{Sz}$ in equations (17) and (21), our model will produce frazil ice in the water column. To see how this works, consider equations (28) and (29) in the absence of advection. Then let $\partial(K_H\,\partial T/\partial z)/\partial z = (F_T/\delta_{BL})\,f_T(z/\delta_{BL})$ and $\partial(K_H\,\partial S/\partial z)/\partial z = (F_S/\delta_{BL})\,f_S(z/\delta_{BL})$, where δ_{BL} is the surface boundary layer thickness. Now approximate $f_T \simeq f_S$. Consider a time interval δt wherein changes in temperature and salinity are δT and δS, respectively. Thus (28) and (29) combine to yield

$$\frac{\delta T}{\delta S} \simeq \frac{F_T}{F_S}$$

From (17) and (21)

$$\frac{\delta T}{\delta S} \simeq \frac{C_{Tz}(T_0 - T)}{C_{Sz}(S_0 - S)}$$

Now, referring to Figure 5, further assume that, initially, T and S are on the freezing line so that, in addition to $T_0 = mS_0$, we also have $T = mS$. To simplify this discussion we neglect the dependence of the freezing temperature on pressure or, effectively, depth. Therefore

$$\frac{\delta T}{\delta S} = m\,\frac{C_{Tz}}{C_{Sz}} \tag{31}$$

Now, if $C_{Tz} = C_{Sz}$, $\delta T/\delta S = m$ so that the water properties remain on the freezing line. However, if $C_{Tz} > C_{Sz}$, which, according to (18*a*), (18*b*), (22*a*), and (22*b*) is the case since $Sc \gg Pr$, then $\delta T/\delta S$ is more negative than previously, and the water becomes supercooled, as illustrated in Figure 5.

If the water becomes supercooled in our calculation, we create frazil ice in the water column and return the T, S properties to the freezing condition. It is easiest to conceptualize the process in terms of discrete states 1 and 2 where state 1 is supercooled according to the process described above and state 2 is after frazil ice has been created and the remaining water has been returned to the freezing state. To accurately treat ice production it is necessary to include the dependence of the freezing temperature on pressure or depth. Thus

$$T_f = mS + nz \tag{32}$$

where, according to *Fujino* [1974], n can be approximated as the constant listed in Table 1. We refer to *Steele et al.* [1989] for a more detailed discussion of frazil ice production and the role of equation (32).

If we let γ = (incremental mass of frazil ice)/(total mass), then the heat and salt balance equations are

$$C_{po}T_1 + L_o = (1 - \gamma)(C_{po}T_2 + L_o) + \gamma C_{pI}T_2$$

$$S_1 = (1 - \gamma)S_2 + \gamma S_I$$

from which, for small γ, we obtain

$$T_2 = T_1 + \gamma L/C_{po} \tag{33}$$

$$S_2 = S_1 + \gamma(S_1 - S_I) \tag{34}$$

where $L = L_F + (C_{po} - C_{pI})T_1$. After combining (33), (34), and the relation, $T_2 = mS_2 + nz$, we obtain

$$\gamma = \frac{C_{po}(mS_1 + nz - T_1)}{L - C_{po}m(S_1 - S_I)} \qquad mS_1 + nz - T_1 > 0$$

$$\gamma = 0 \qquad mS_1 + nz - T_1 < 0 \tag{35}$$

In the numerical model we now interpret $\delta T = T_2 - T_1$ and $\delta S = S_2 - S_1$ as the changes occurring in the time step δt. After γ is obtained from (35), δT and δS are obtained from (33) and (34), respectively. The frazil ice is immediately removed from the water column and added to the surface ice sheet. The rate of frazil ice accumulation at the surface is then

$$W_{FR} = \delta t^{-1} \int_H^0 \gamma\, dz$$

where H is the depth of the water column.

Equations (33), (34), and (35) are in lieu of a more detailed model where one would solve for frazil ice formation, a frazil ice concentration profile, and subsequent vertical buoyant drift to the surface.

5. Decoupled, One-Dimensional, Ice Model Calculations

Comparison With the Calculated Results of Maykut and Untersteiner

In this section we wish to compare the present model results with the results of the high-resolution ice model of MU. The ice model is decoupled from the ocean model by externally specifying the oceanic heat flux and temperature, F_T and T_0. Furthermore, we set $A = 1$. Note that ice dynamics are irrelevent to the thermodynamics in the decoupled mode; furthermore, all of the results in sections 3 and 4 are not used at all here.

TABLE 2. Prescribed Standard Forcing

Symbol	Variable	Jan.	Feb.	March	April	May	June	July	Aug.	Sept.	Oct.	Nov.	Dec.	Year
SW	incoming shortwave radiation, kcal cm^{-2}	0	0	1.9	9.9	17.7	19.2	13.6	9.0	3.7	0.4	0	0	75.4
LW	incoming longwave radiation, kcal cm^{-2}	10.4	10.3	10.3	11.6	15.1	18.0	19.1	18.7	16.5	13.9	11.2	10.9	166.0
Q_{SI}	flux of sensible heat, kcal cm^{-1}	1.8	0.76	0.72	0.29	−0.45	−0.39	−0.30	−0.40	−0.17	0.10	0.56	0.79	2.71
Q_{LI}	flux of latent heat, kcal cm^{-1}	0	−0.02	−0.03	−0.09	−0.46	−0.70	−0.64	−0.66	−0.39	−0.19	−0.01	−0.01	−3.20
α_s*	snow albedo	...	...	0.83	0.81	0.82	0.78	0.64	0.69	0.84	0.85	...	...	...

Compiled by *Fletcher* [1965] and used by *Maykut and Untersteiner* [1971]. To convert kcal cm^{-2}/month to W m^{-2} for a 30-day month, multiply the tabulated values by 1.346.

*MU used values interpolated from this row except when snow began to melt after which the albedo varied linearly from the last interpolated, dry snow value to the value 0.64 when the snow had completely melted. We followed the same procedure for our first calculation after which equation (36) was used instead.

We follow MU, who used the monthly averaged heat budget of *Fletcher* [1965], which they spread over twelve months where a month is taken as 30 days. The values are tabulated in Table 2. The Stefan-Boltzmann constant was taken as 5.78×10^{-8} W m^{-2} K^{-4} instead of the commonly accepted value of 5.67×10^{-8} W m^{-2} K^{-4}; most of the difference can be attributed to the fact that the calculation is based on a 360-day year. Thus in this paper, much of the bulk formulas in Appendix A are bypassed except for the fact that we will later use them to correct Fletcher's values for open water fluxes when $A < 1$.

We also follow MU in prescribing a snow accumulation of 30 cm between August 20 and October 30, then a further increase of 5 cm to April 30 and additional 5 cm during May; however, snow accumulation is terminated if the surface temperature reaches the melting point.

The ocean heat flux at the base of the ice was fixed at 1.5 kcal cm^{-2} year^{-1} = 2.02 W m^{-2}, a number which is justified in MU but has been disputed by *Morrison and Smith* [1981] (they also cite G. A. Maykut (unpublished work, 1981) in corroboration of a lower heat flux). Nevertheless, we use this value to facillitate the comparison of results. For comparison with Table 2 this is equivalent to 0.125 kcal cm^{-2} month^{-1}; variations in such a relatively small number have been shown by MU and by *Semtner* [1976*a*] (see also Table 3 and Figure 8) to have a significant effect on ice thickness.

We note that instead of using the latent heats defined in (10*b*) and (15*c*), MU fixed L_3 and L_0 at values corresponding to brine fractions $r = 0$ and 0.2, respectively. Semtner alludes to the fact, and we agree, that MU do not globally conserve energy by this procedure. Nevertheless, we will incorporate this as a temporary change only for the calculation cited next.

The model was run for thirty years; the time step was 1 hour, and the ocean vertical grid spacing was 5 m except for the upper four grid points which decreased logarithmically to 0.5 m. After attainment of equilibrium the model yielded an annual mean thickness about 15% higher than the MU result. We have not been able to identify the reason for the difference in the two calculations; it could be due to differences in the model formulation, the numerical algorithm, or to undiscovered differences in interpolating the thermodynamic forcing. From Semtner's results it would not seem that resolution is responsible. We have also checked extensively for code errors in our model. The difference is corrected by either a 2% decrease in albedo or by an 8% decrease in snow and ice heat conductivity and yields results almost identical to those shown in Figure 6.

Albedo Model

We now restore the model, as represented by sections 1–4 and by Table 1. In addition, we depart from the use of the albedos listed in Table 2 since, in future application, the model itself should determine these values. Therefore we substitute the following relations:

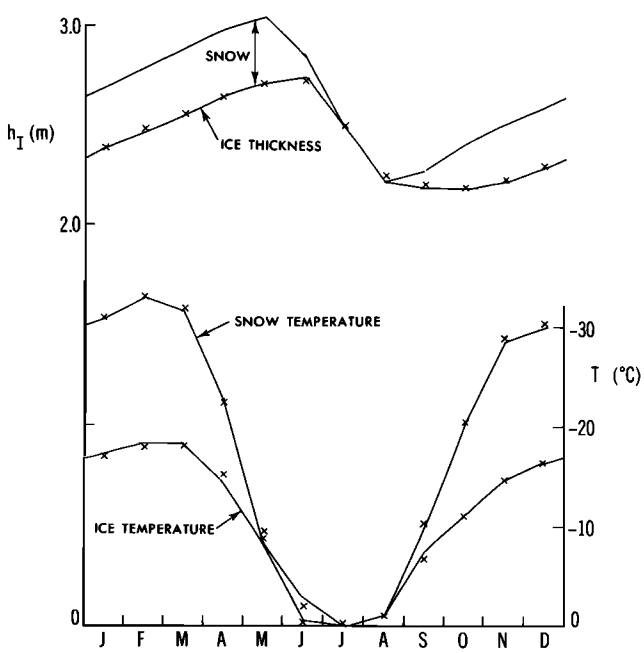

Fig. 6. The monthly averaged, equilibrium values of snow thickness and the ice thickness and the temperature of the snow and ice surfaces. The crosses are the monthly averaged values calculated by *Maykut and Untersteiner* [1971]. Ice ablates at the top at the rate of about 0.5 m year^{-1}, which is balanced by accretion of an equal amount at the bottom.

TABLE 3. The Effect of Albedo Variations, Ice Salinity, Ocean Heat Flux, and Trapped Surface Water on the Annual Mean Ice Thickness

α_I	F_T, W m^{-2}	S_I, ppt	h_{sw}, m	$\langle Ah_I \rangle$, m	Remarks
0.8215/0.73/0.64	2.02	3.	0	2.42	Figure 6
0.82/0.73/0.64	2.0	3.	0	2.38	standard for this table
0.84/0.73/0.64	2.0	3.	0	3.16	
0.82/0.75/0.64	2.0	3.	0	2.78	α_I sensitivity
0.82/0.73/0.66	2.0	3.	0	2.79	
0.82/0.73/0.64	0.0	3.	0	4.16	F_T sensitivity
0.82/0.73/0.64	2.0	0	0	2.26	S_I sensitivity
0.82/0.73/0.64	2.0	3.	0.10	3.27	h_{sw} sensitivity

Column heads are α_I, dry snow albedo/wet snow albedo/bare ice albedo; F_T, oceanic heat flux; S_I, ice salinity; h_{sw}, maximum standing meltwater; $\langle Ah_I \rangle$, annual mean, area-averaged ice thickness.

For snow-covered ice with no melting (dry snow)

$$\alpha_I = 0.82 \tag{36a}$$

For melting snow (wet snow)

$$\alpha_I = 0.73 \tag{36b}$$

For bare ice

$$\alpha_I = 0.64 \tag{36c}$$

Using (36), the annual mean ice thickness was about 2% too low compared to the MU results; an adjustment of the value 0.82 to 0.8215 effected nearly exact correspondence with the MU result, as shown in Figure 6. From these results and from the more deliberate sensitivity studies in the next section it is apparent that our knowledge of many of the physical parameters are not precise enough to preclude the fact that any model will have to be tuned so that calculated results agree with observation.

Aside from the information displayed in Figure 6, one finds here, as in MU, that congelate ice is accreted on the underside of the ice sheet at a relatively uniform rate, with some reduction in the summer. On the other hand, ice is melted on the top surface entirely during June, July, and the first part of August. During a single annual cycle the total bottom accretion of ice and the equal amount of surface melting is about 50 cm. Thus a particle frozen at the bottom will migrate to the top over a period of 4–5 years.

Sensitivity Studies

Continuing with the decoupled ice model, we wish to determine the sensitivity of the model to some of the model parameters. The results are somewhat cryptically reported in Table 3, where we measure sensitivity only by the annual average of the area-averaged depth $\langle Ah_I \rangle$. In Table 3 the first row is identical to the parameters used in Figure 6, where the dry snow albedo is tuned (with four-place precision!) to compare with the MU calculations. The second is the same, with the dry snow albedo and oceanic heat flux rounded to two-place precision; this case will, hereinafter, represent the "standard" case.

Following the standard case in Table 3 are cases where the dry snow albedo, the wet snow albedo, and the bare ice albedo are increased successively by the amount 0.02; this amount increases the annual near-ice depth by about 30% in the case of the dry snow albedo increase and 15% in the other cases.

The next case shows the effect of specifying zero ocean heat flux, which yields an 80% increase in annual ice depth; this result is in accordance with the similar sensitivity studies by MU and *Semtner* [1976*a*] to which the reader is referred for a more extensive range of ocean heat flux variation. As previously discussed, the actual annual mean heat flux in the central Arctic may, in fact, be much smaller than the standard chosen by MU.

The next case shows the effect of decreasing ice salinity from 3 ppt to 0. This results in only a 5% decrease in mean ice depth. However, the lag effect of increasing the effective heat capacity of ice when $S_I = 3$ ppt does change the detailed, late summer and fall distribution of the snow and ice surface temperatures in Figure 6 such that they are more closely in agreement with the MU results, as compared to the calculations (not shown) when $S_I = 0$.

The next case in Table 3 shows the result of increasing the maximum depth of standing water to a value of $h_{sw} = 0.10$ m, resulting in a 40% increase in the mean ice depth. Instead of summer meltwater being lost from the system it is retained and readily available near the surface for refreezing in the fall. At this point we note that MU include the possibility of shortwave radiative penetration into the near-surface portion of bare ice. This shortwave energy converts ice into brine pockets; this water is also retained and readily available near the surface for refreezing in the fall. This process is not dissimilar to simply retaining water on the surface. In fact, we obtain very similar results to the MU case of 17% shortwave penetration by setting $h_{sw} = 0.06$ m in our model. Note, however, that the direct effect of standing water pools, although it is a simplification to spread the water uniformly, might be as important or more important than shortwave penetration.

We next study the thermodynamic effects of the compactness A. We also wish to assess the effects of Φ_F and Φ_M in equation (4), which are rather uncertain parameters. To be consistent with the previous results we continue to use the heat flux values of Table 2 and the albedoes from (36), together with the value, $\alpha_o = 0.10$, for open water. However, we do use equations (A7)–(A10) to correct the sensible and latent heat fluxes of Table 2 to obtain the corresponding open water fluxes.

In order to create $A < 1$ in a one-dimensional context we replace the advection term in (3) and (4) by Ah_I div $\mathbf{V}$ (= $A\, h_I\, \partial U_{Ii}/\partial x_i$). In Figure 7, for the standard values $\Phi_M = 0.5$ and $\Phi_F = 4$ and for the ice divergence, div $\mathbf{V} = 0.0$, 1.0, 2.0, 3.0, and 4.0×10^{-9} s^{-1}, we show the annual march of the area-averaged ice thickness Ah_I, the concentration A, the

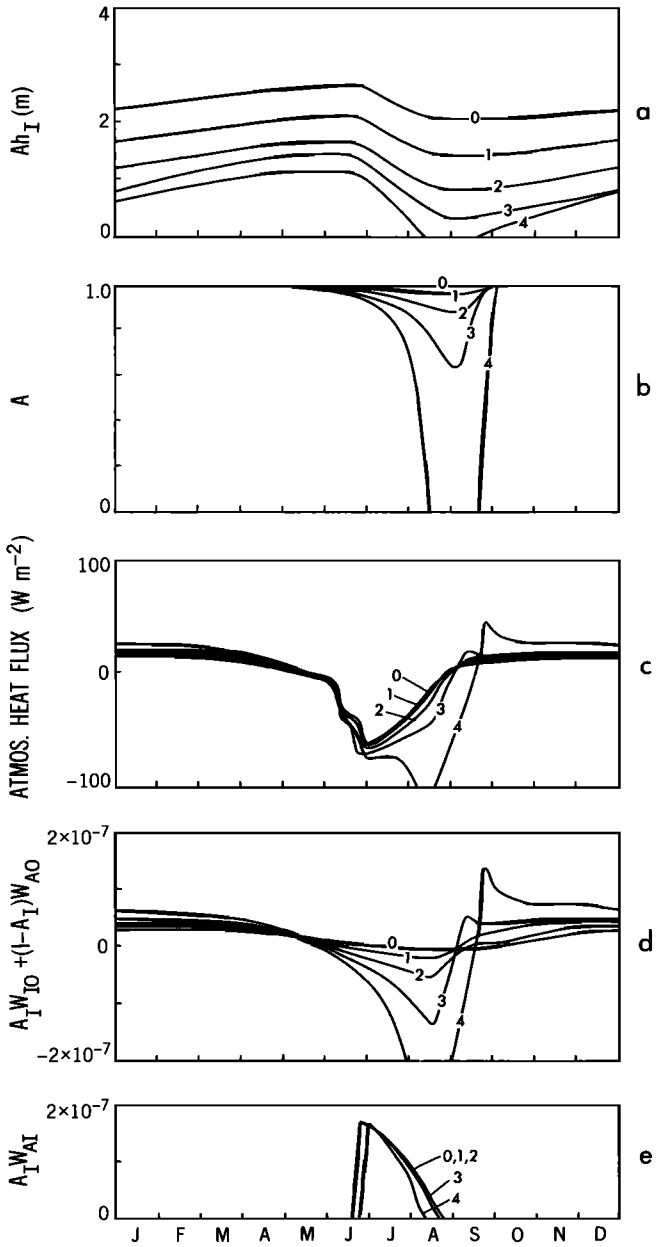

Fig. 7. The final year of a 30-year integration: (*a*) the area-averaged ice thickness; (*b*) the concentration; (*c*) the net atmospheric heat flux; (*d*) the net ice-ocean freeze/melt rate; (*e*) the ice-atmospheric melt rate. The calculations include the effects of divergence, div V; contours of constant div V are labeled in units of 10^{-9} s^{-1}. The values Φ_M and Φ_F in equation (5) were set at 0.5 and 4.0, respectively. Annual periodicity prevails for div V $\leq 2.1 \times 10^{-9}$ s^{-1}. See text for discussion of larger values.

net surface heat flux $AQ_{AI} + (1 - A)Q_{AO}$, the net ice-ocean plus atmosphere-ocean freeze rate $AW_{IO} + (1 - A)\ W_{AO}$, and the atmosphere-ice melt rate AW_{AI}. The results are for the last year of a 30-year integration.

Note that positive ice divergence creates a negative tendency for Ah_I in (3) and A in (4). In all but the summer months this negative tendency is counterbalanced by refreezing, so that A is maintained very close to unity. However, in the summer months, shortwave radiation is absorbed more efficiently by open leads (where the albedo, α_O

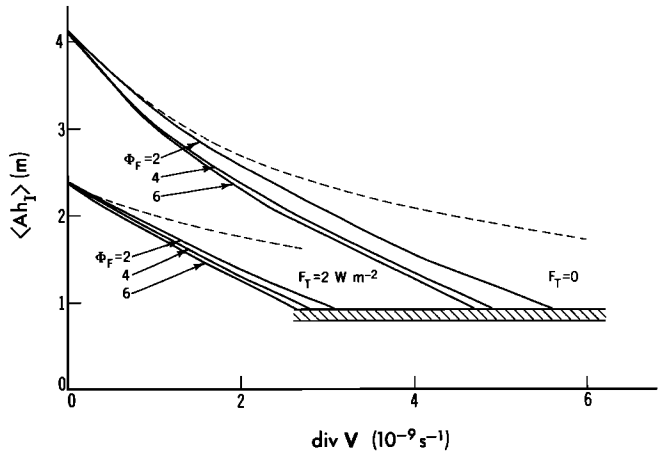

Fig. 8*a*. Annual and area-averaged ice thickness $\langle Ah_I \rangle$ for a range of values of div V and of Φ_F. Φ_M is fixed at the value 0.5; see equations (4) and (5). The dashed curve is a calculation where (4) is numerically overwritten so that $A = 1$; this curve represents only the effects of ice being transported out of the region. Annual periodicity prevails for values denoted by solid curves. See text for discussion of values denoted by hashed marks.

= 0.10), so that melting and open water creation is enhanced. For div V $\leq 2.0 \times 10^{-9}$ s^{-1} an annual cycle is established. When div V = 2.5×10^{-9}, periodicity is not obtained throughout the 30-year run, and summer ice-free conditions are obtained every 3 to 5 years. When div V = 3.0×10^{-9} s^{-1}, a 3-year cycle is established, with ice-free conditions appearing every 3 years. For div V = 3.5 and 4.0×10^{-9} s^{-1} a 2-year cycle is obtained, with ice-free summers every other year. For larger values of div V an annual cycle is reestablished, and the summers are all free of ice.

In Figures 8*a* and 8*b* the annual average values of Ah_I, denoted $\langle Ah_I \rangle$, are plotted as functions of div V for $\Phi_M = 0.5$ and $\Phi_M = 1.0$, respectively, and for various values of Φ_F. The portions of the curves denoted by solid lines indicates that a repeating, annual cycle has been established; multiyear cycles occur where the curves are dotted or where there are hashed marks. We also show the result (dashed curve) where we overwrite (4) and set $A = 1$; the variation of $\langle Ah_I \rangle$ is then due entirely to the transport of ice out of the region.

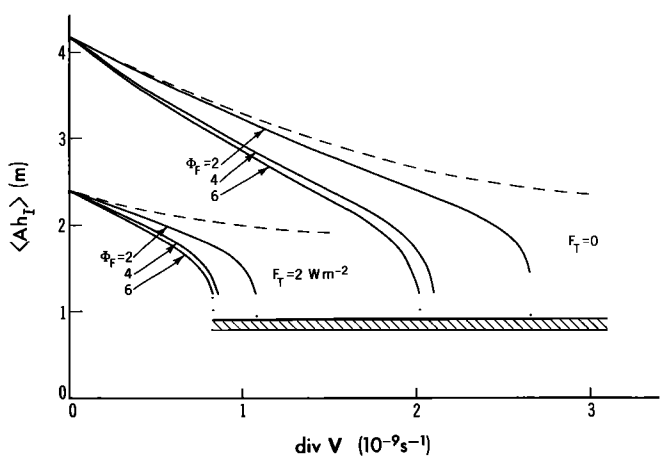

Fig. 8*b*. The same as Figure 8*a* except that $\Phi_M = 1.0$. Note change of abscissa scale relative to Figure 8*a*. Annual periodicity prevails for values denoted by solid curves. See text for discussion of values denoted by dotted lines or by hashed marks.

TABLE 4. Seasonal and Annual Mean Profiles North of 83°N

Depth, m	Winter (FMA)		Spring (MJJ)		Summer (ASO)		Fall (NDJ)		Annual Mean	
	T, °C	S, ppt	T, °C	S, ppt	T, °C	S, ppt	T, °C	S, ppt	T, °C	S, ppt
0.	−1.71	31.41	−1.67	31.24	−1.64	30.86	−1.70	31.32	−1.680	31.208
10.	−1.71	31.41	−1.67	31.24	−1.64	30.86	−1.70	31.32	−1.680	31.208
20.	−1.72	31.42	−1.68	31.25	−1.65	30.91	−1.70	31.32	−1.688	31.225
30.	−1.72	31.44	−1.69	31.26	−1.66	30.95	−1.70	31.33	−1.693	31.245
50.	−1.72	31.59	−1.64	31.48	−1.60	31.40	−1.69	31.71	−1.663	31.545
75.	−1.56	32.51	−1.52	32.40	−1.48	32.37	−1.59	32.83	−1.538	32.528
100.	−1.48	33.11	−1.49	32.86	−1.45	32.86	−1.51	33.35	−1.483	33.045
125.	−1.34	33.52	−1.48	33.12	−1.37	33.12	−1.35	33.55	−1.385	33.327
150.	−1.17	33.86	−1.23	33.46	−1.20	33.53	−1.01	33.95	−1.153	33.700
200.	−0.46	34.42	−0.53	34.20	−0.57	34.28	−0.29	34.43	−0.463	34.333
250.	0.07	34.65	0.06	34.52	0.04	34.57	0.22	34.63	0.098	34.593
300.	0.53	34.79	0.64	34.74	0.52	34.73	0.50	34.75	0.548	34.753
500.	0.54	34.90	0.57	34.87	0.51	34.87	0.47	34.87	0.522	34.878
1000.									−0.188	34.735
1500.									−0.400	34.950
2000.									−0.428	34.958
OBS		11-8		26-20		30-20		10-23		

Numbers shown in the OBS row are the number of salinity observations at depths of 0 and 500 m. The annual mean profile includes values at 1000–2000 m, where the total number of salinity observations were 72 and 19, respectively. The number of temperature observations in the top 500 m are larger by a factor of 5 or more. T, temperature; S, salinity; OBS, observations; FMA, Feb., March, April; MJJ, May, June, July; ASO, Aug., Sept., Oct.; NDJ, Nov., Dec., Jan.

Note the scale of the abscissa of Figure 8*b* relative to Figure 8*a*. The point where ice-free water is formed occurs at smaller values of div V when $\Phi_M = 1.0$ than when $\Phi_M = 0.5$.

The overall result is that, for $\Phi_F > 2$, the results are fairly insensitive to this otherwise uncertain parameter. Future attention should be directed at a more rational determination of Φ_M to which the calculations are sensitive.

6. The Ice-Ocean Coupled Model

We now couple the ice model with our ocean model, and we will continue to use the same atmospheric forcing as in the previous section; however, the constraint on sea surface temperature and heat flux will be relaxed.

In this coupled model it is the wind and resulting ice motion that forces the oceanic mixed layer and enables the ice to interact with the mixed layer via heat and salinity fluxes. A choice of wind speed of 6 m s^{-1} is based on the monthly climatology of *Gorshkov* [1983]. Variability of the wind is of some importance to the mixing process [*Klein*, 1980], so we have allowed the wind to vary sinusoidally with an amplitude of $(\pi/2)$ 6 m s^{-1}, a period of 4 days, and a constant wind direction, a rather crude representation of a wind time series.

Some inventiveness is required to overcome ignorance of horizontal advection of temperature and salinity in a one-dimensional representation of the model. In Table 4 are values obtained from the Master Oceanographic Observational Data Set in the region north of 83°N. The data are sparse and subject to spatial and temporal sampling errors. In the absence of advective processes one can only hope to model thermodynamic details in the mixed layer. We therefore plot the annual mean temperature and salinity data points in Figure 9. Our strategy will be to approximate these mean values while at the same time calculating the time-varying values with the model. As a lower boundary condition at $z = -78$ m, we set $T = -1.54$°C and $S = 32.7$ ppt. At this lower boundary point, calculations reveal that the model-generated mixing coefficients are effectively null. However, we do use a "background" coefficient, which is discussed below. This will result in a salinity flux at the base of the mixed layer. However, the salinity flux at the surface

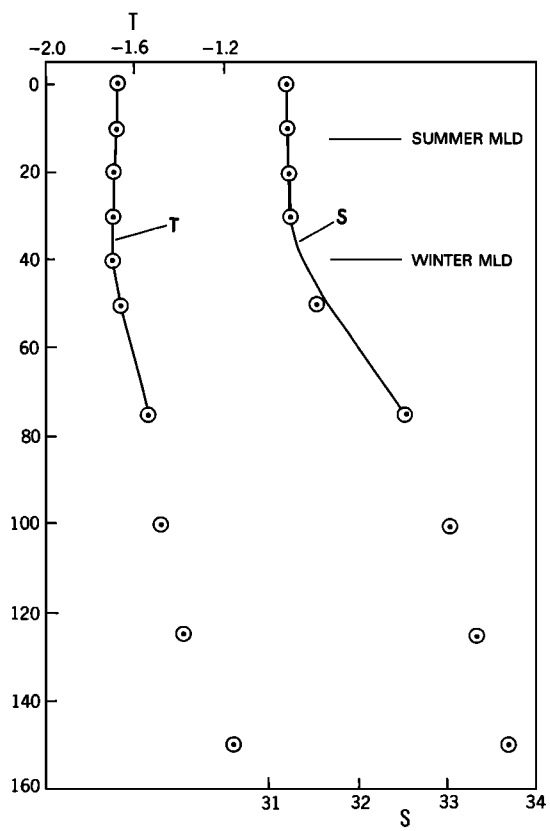

Fig. 9. The annual mean temperature and salinity data, the open circles, taken from Table 4. The solid curves are the annual mean values calculated by the model. The minimum, summer and maximum, winter mixed layer depth (MLD) calculated by the model are indicated.

is very small; brine rejection due to freezing is balanced by meltwater runoff in the summer months, but there is some residual flux due to the removal of ice through the div **V** term. Therefore the combined fluxes at the surface and base of the mixed layer result in a slow salinity increase which, it turns out, does not significantly affect the thermal results. Nevertheless, in the results to be presented we have simply removed salt uniformly throughout the water column so that equilibrium is attained and the calculated, annual mean salt storage is as shown in Figure 9. In the central Arctic it is quite likely that this would be supplied by horizontal advection, whose source is freshwater runoff from land.

There is no need to tamper with the temperature field, since the surface value is locked in at the freezing value. Furthermore, one suspects that mixed layer advection of temperature is small in the central Arctic, since surface temperature variations are small.

For ice-free oceans, thermocline vertical mixing coefficients are thought to be in the range of 0.1 to 0.3 $cm^2\ s^{-1}$ [*White and Bernstein*, 1981; *Martin*, 1985]. For comparison, the mixing coefficients produced by the closure model are of the order of 100 $cm^2\ s^{-1}$ in the mixed layer but are essentially null below the mixed layer. We therefore choose a "background" mixing coefficient of 0.2 $cm^2\ s^{-1}$; this results in an annual mean heat flux of 0.33 W m^{-2} at the base of the mixed layer. The annual mean temperature profile is plotted in Figure 9. Variations in the background mixing coefficient do not change the profile significantly but do reveal a nearly linear relation between the prescribed thermocline mixing coefficient and heat flux at the base of the mixed layer.

The annual mean temperature and salinity profiles indicate that the calculated mixed layer depth is about right; the summer and winter extremes of mixed layer depth are denoted in Figure 9.

Figures 10–15 contain plots of key variables as functions of time. The empirical factors Φ_M and Φ_F were to set to the values 0.5 and 4.0, respectively. Figures 10*a*–15*a* contain the area-averaged ice thickness and concentration; Figures 10*b*–15*b* show various components of freezing and melting rates at the surface and at the base of the mixed layer; Figures 10*c*–15*c* are the oceanic heat flux at the surface and at the base of the mixed layer. Finally, Figures 10*d*–15*d* and Figures 10*e*–15*e* are time depth plots of the temperature and salinity. The ratio of frazil ice to congelate ice production is denoted by *F*/*C*.

The first three figures, 10, 11, and 12, are calculations where div **V** = 2 × 10^{-9} s^{-1}, h_{sw} = 0, and S_I = 3 ppt and where the parameter b is set to 0, 1.5, and 3.0, respectively. The motivation for this evaluation of the effects of b is the following: The value b = 0 corresponds to the assumption which generally prevails in the literature on ice models [e.g., *Josberger*, 1983; *Ikeda*, 1986], whereas the value b = 3.0 is essentially the value recommended by *Yaglom and Kader* [1974]. However, *McPhee et al.* [1987] found a match with marginal ice zone measurements when he used a value close to b = 1.5. A possible justification for a value lower than that obtained by Yaglom and Kader is simply that the statistics of ice roughness are unlike the roughness distributions created in laboratory flows. In any event we wish to understand the consequences of variations in b and, hopefully, to see if we can discriminate an independent choice of this variable.

Now, in Figures 10*c*, 11*c*, and 12*c* we note that the heat flux at the base of the mixed layer varies slightly around the annual mean value of 0.33 W m^{-2}. However, the surface values vary greatly as a function of time and as function of b. For b = 0 the annual mean surface heat flux equals the base value. For b equal to 1.5 and 3.0 the annual mean surface heat fluxes are 2.14 and 2.40 W m^{-2}, respectively; the

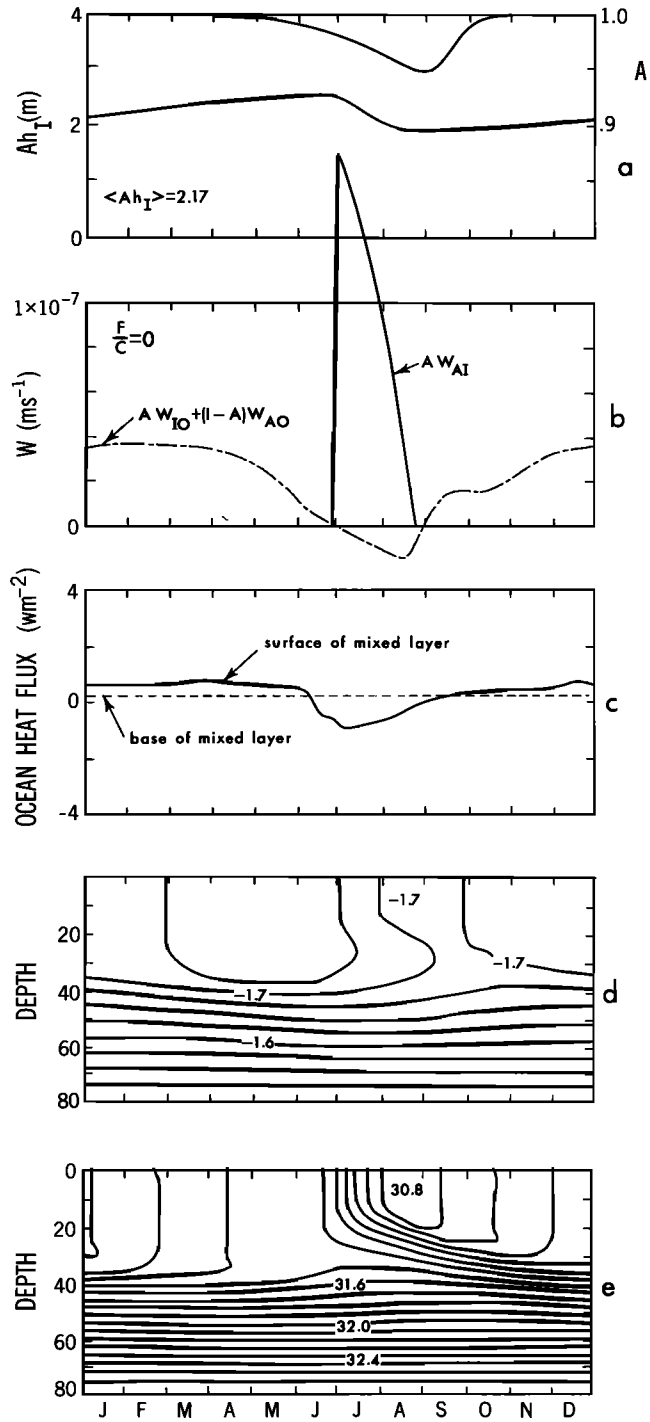

Fig. 10. Coupled ice-ocean calculation where b = 0 in equations (18*b*) and (21*b*), div **V** = 2 × 10^{-9} s^{-1}, and h_{sw} = 0. (*a*) Ah_I (left scale) and A (right scale). (*b*) Ice surface melt rate, ice bottom accretion rate (dot-dashed curve), and frazil ice production rate. (*c*) Ocean heat flux at the surface and at the base of the mixed layer. (*d*) Contours of temperature; contour interval = 0.25°C. (*e*) Contours of salinity; contour interval = 0.1 ppm. The annual average value of Ah_I is given in Figure 10a, and the ratio of frazil to congelate average freeze rate is given in Figure 10b.

difference between these values and the base value of 0.34 W m^{-2} is due to frazil ice production in the water column, with consequent release of latent heat. The discussion relative to equation (31) in section 4 provides the reason why the value $b = 0$ does not produce frazil ice whereas the values $b > 0$ do produce frazil ice. Furthermore, examination of (18*a*), (18*b*), (22*a*), and (22*b*) will reveal that $C_{Tz}/C_{Sz} \simeq (Sc/Pr)^{2/3} = (\alpha_t/\alpha_s)^{2/3}$, and therefore the rate of frazil ice production should not be overly sensitive to b except when b is quite close to zero; this is more or less the case, as seen in of

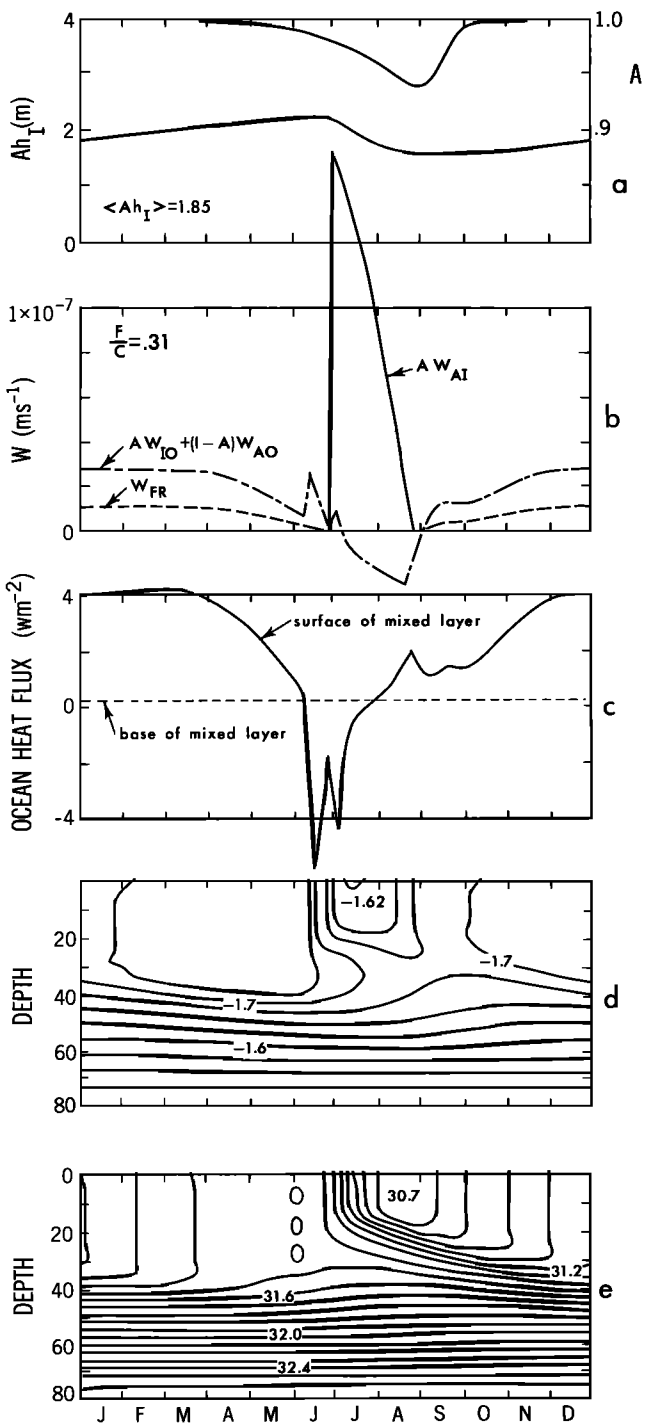

Fig. 11. The same as Figure 10 except that $b = 1.5$. Frazil ice is now created and plotted in Figure 11*b*. Because of the depth dependent, freezing temperature relation, equation (30), frazil ice production is confined to the upper 3 to 4 m.

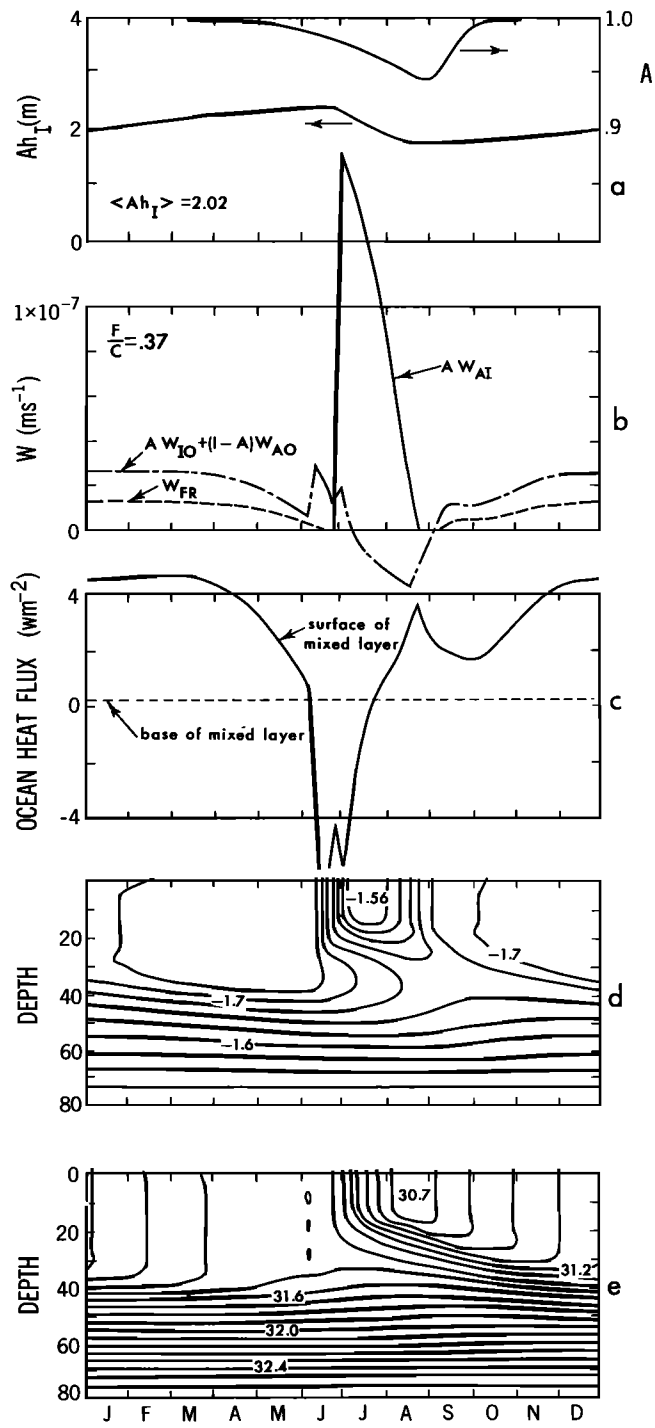

Fig. 12. The same as Figure 10 except that $b = 3.0$.

Figures 11*b* and 12*b*. We now note that frazil ice production is confined to the top 3–4 m, with the maximum at the topmost layer. This is largely governed by equation (32), wherein n is a negative number and T_f is lower in deeper water. A run where $n = 0$ produced nearly the same total amount of frazil ice, but production was distributed through most of the mixed layer.

In Figure 13 we show results where the frazil ice production is not enabled at all, and the water column is supercooled. At the surface in winter the water is supercooled by about 0.01°C. The annual area-averaged ice thickness is increased by 18% over that in Figure 11.

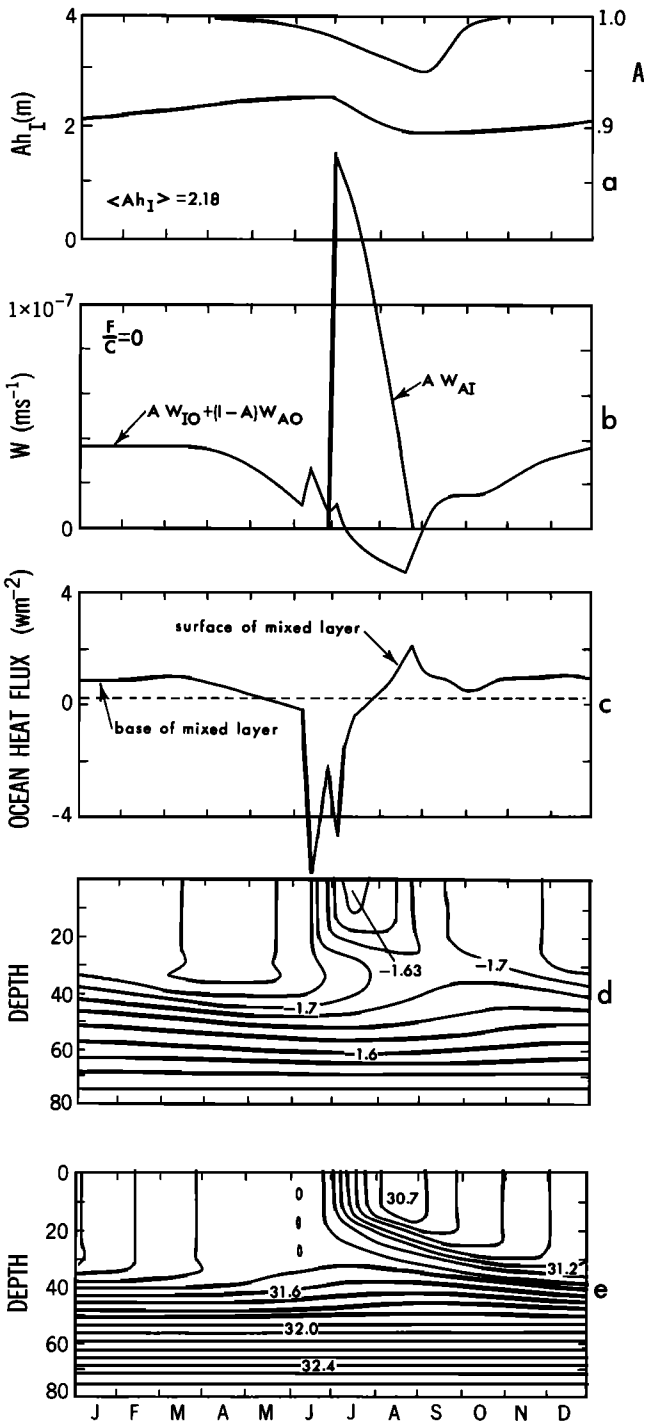

Fig. 13. The same as Figure 11 (b = 1.5) except that frazil ice creation has not been enabled so that, except for summer months, near-surface water is supercooled.

A prominent difference in the three cases, b = 0, 1.5, and 3.0, is the summertime mixed layer temperature signal; as b increases, the summertime temperature increases. The summertime salinity flux is approximately the same in all three cases, as is the near-surface salinity. However, because of the increased resistance to salinity flux for larger b (see (21), (22a) and (22b)), the salinity S_0 on the ice side of the molecular sublayer is significantly decreased. For example, the average July values are S_0 = 31.08, 29.80, and 28.68 when b = 0, 1.5, and 3.0, respectively, and according to (33), T_0 = −1.69, −1.62, and −1.56. This then forces the water column to be at a higher temperature as b increases; the process is enhanced by the fact that the molecular sublayer resistance to heat flux is much less than the resistance to salinity flux, since $Pr \ll Sc$.

In Table 5 we compare the seasonally averaged model surface temperatures and salinities to the similarly averaged observed values from Table 4. From these results one concludes that, certainly, $b > 0$ and, in fact, the comparison would seem to favor values in excess of the value 1.5 obtained by *McPhee et al.* [1987] to match data for rapidly

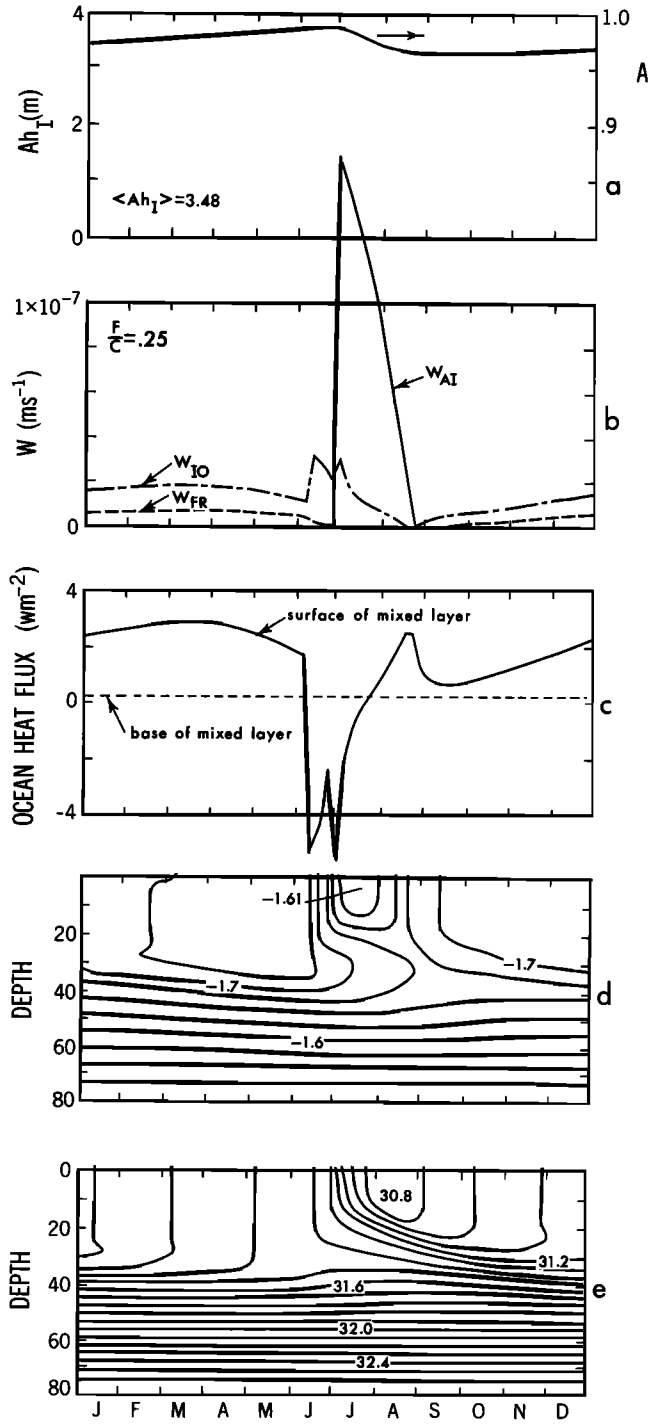

Fig. 14. The same as Figure 11 except that div **V** = 0 and, consequently, A = 1.

melting ice in the marginal ice zone. Note, however, that these results are dependent on the choice of z_0 and possibly on details of the statistics of the roughness distribution.

7. Increased Ice Divergence

Ice divergence was included in the model as a means of creating leads and as a means of testing the formulation for ice concentration. It does create open water. However, a primary role of ice divergence is simply to export ice out of the model domain. Now that the model is more or less

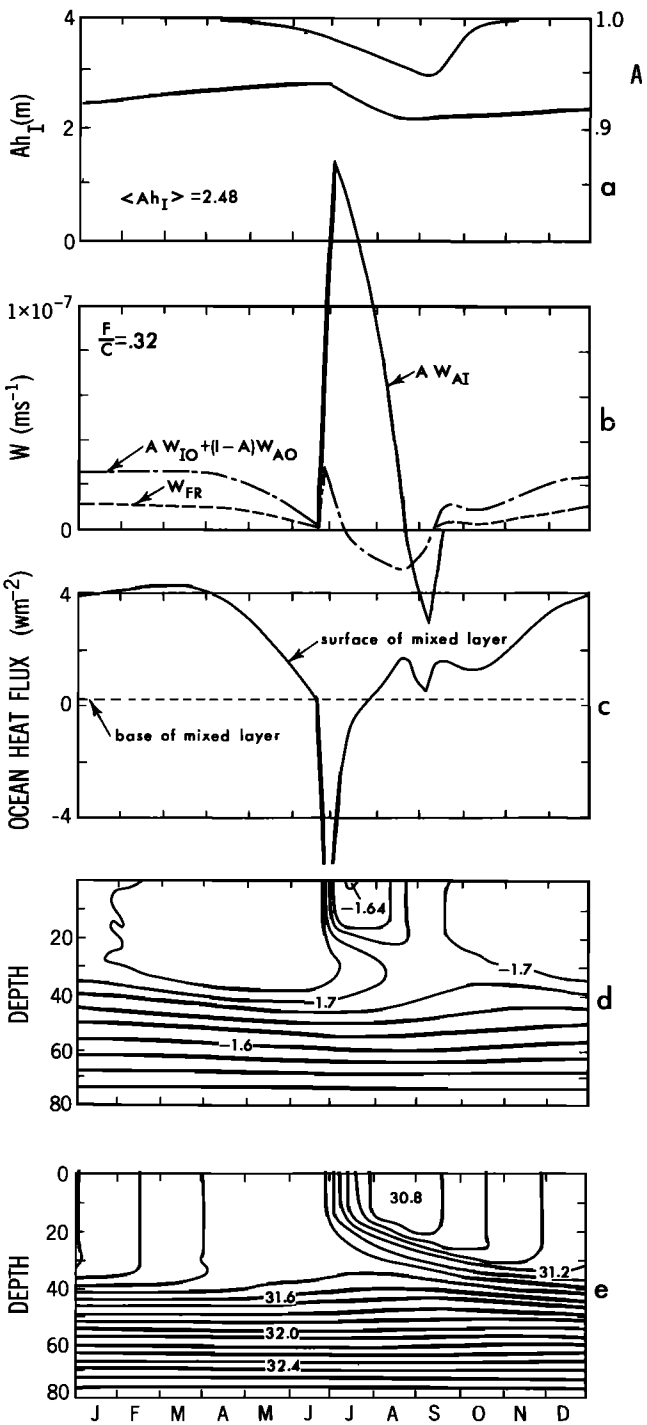

Fig. 15. The same as Figure 11 except that $h_{sw} = 0.1$. Note that the surface melt rate (solid curve in Figure 15b) has a negative portion, indicating melt pool freezing.

TABLE 5. A Comparison of Seasonally Averaged Model Surface Temperatures, and Salinities, and the Data of Table 4

Season	*b* 0	*b* 1.5	*b* 3.0	Data
		Temperatures		
FMA	−1.70	−1.70	−1.71	−1.71
MJJ	−1.70	−1.68	−1.66	−1.67
ASO	−1.69	−1.67	−1.66	−1.64
NDJ	−1.69	−1.69	−1.69	−1.68
		Salinities		
FMA	31.48	31.38	31.38	31.41
MJJ	31.32	31.31	31.33	31.24
ASO	30.91	30.83	30.85	30.86
NDJ	31.12	31.13	31.13	31.32

The seasonal definitions follow *Levitus* [1982], see Table 4.

complete we ask the question: What are reasonable values of div **V**?

From the ice drift measurements analyzed by *Colony and Thorndike* [1984] we approximate div $\mathbf{V} \simeq 4.5 \times 10^{-9}$ s^{-1} for the central Arctic and 3.0×10^{-9} for the entire Arctic basin. *Vinje and Finnekasa* [1986] estimated the ice transport through the Fram Straits at 0.16×10^6 m^3 s^{-1}, a number close to other estimates that are cited in their paper. Assuming an average ice thickness of 3 m, we obtain div $\mathbf{V} = 6.5 \times 10^{-9}$ s^{-1}. (This is equivalent to ice production of 0.64 m y^{-1}, a number which is somewhat larger than the bottom ice accretions rate, ~0.55 m y^{-1}, according to the MU model and the present model.)

We have surveyed the effect of div **V** for the decoupled ice model. In the coupled model we have used the value, div $\mathbf{V} = 2 \times 10^{-9}$ s^{-1}. Our results yield an annual mean ice thickness of around 2 m. Now if we repeat the run of, say, Figure 11 with a larger div $\mathbf{V} = 4 \times 10^{-9}$ s^{-1}, we obtain $\langle Ah_I \rangle = 0.89$ m instead of 1.85 and instead of the observed 3.0 m [*Bourke*, 1987]!

The answer to this apparent dilemma resides in the paper by *Maykut* [1982], where it is shown that, if one takes into account the thickness distribution $g(\bar{h})$, the thinner ice will grow much faster in the winter, since it offers less resistance to heat transfer than does thicker ice. We have used $h_I = \int \bar{h}\, g(\bar{h})\, d\bar{h}$ to represent ice thickness. However, for the thickness used in the heat conduction equation we should instead use $\int \bar{h}^{-1}\, g(\bar{h})\, d\bar{h}$. This idea requires a little development, however, since heat conduction is not uniquely dependent on thickness. For this purpose we neglect the heat capacity of the ice and snow so that, referring to Figure 4, we have

$$\bar{Q} \equiv \bar{Q}_s = \bar{Q}_{IO} = \bar{Q}_{I2} = k(\bar{T}_3 - T_0)/\bar{h}$$

where we use the tildes to represent local values. Here k and $\bar{h}$ represent composite snow and ice values. Thus the actual heat flux is

$$Q = \int_0^\infty \frac{k}{\bar{h}} (T_3(\bar{h}) - T_0) g(\bar{h})\, d\bar{h}$$

where we note that T_3 is a function of $\bar{h}$ for a given atmospheric forcing. We now define a conduction correction factor G such that

$$Q = G \frac{k}{h_I} (T_3(h_I) - T_0) \qquad (37)$$

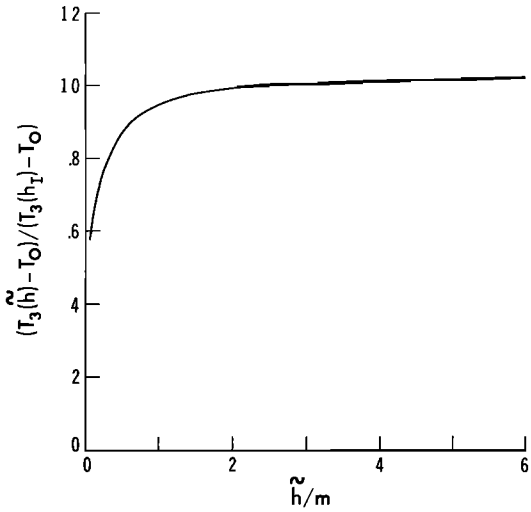

Fig. 16. The ratio of the temperature drop across the ice, based on local thickness, to the temperature drop based on the average thickness.

Combining the above two equations yields

$$G = \int_0^\infty \frac{h_I}{\tilde{h}} \left[\frac{T_3(\tilde{h}) - T_0}{T_3(h_I) - T_0} \right] g(\tilde{h})\, d\tilde{h} \tag{38}$$

We now run a simplified model, valid for winter conditions, which is a balance between incoming and outgoing long-range radiation, sensible heat flux (see Appendix A), and Q_{I2}. The atmospheric temperature T_A was allowed to vary from $-30°$ to $-10°$, and $\tilde{h}$ varied in the range $0 < \tilde{h} < 6$ m and $T_0 = -1.8°C$. The ratio $(T_3(\tilde{h}) - T_0)/(T_3(h_I) - T_0)$ is plotted in Figure 16, where we take $h_I = 3$ m, although the result is hardly sensitive to this value. The curve in Figure 16 is essentially independent of T_A. It is also weakly dependent on $\tilde{h}$ except near $\tilde{h} = 0$. As a consequence of this result

$$G = \int_\varepsilon^\infty \frac{h_I}{\tilde{h}}\, g(\tilde{h})\, d\tilde{h} \tag{39}$$

where, if $g(\tilde{h})$ is finite for $\tilde{h} \to 0$, then the cutoff, $\varepsilon = 0.1$ m, accounts for the sharp decrease in the temperature ratio in Figure 16.

To develop some feel for the magnitude of G, let $g(\tilde{h}) = 0$ where $\tilde{h} < 1$ m and $g(\tilde{h}) = 0.25$ where $1 \text{ m} < \tilde{h} < 5$ m. We then obtain the value $G = 1.21$ from (39). Now provide some young ice so that $g(\tilde{h}) = a$ when $\tilde{h} < 1$ m and $g(\tilde{h}) = 0.25$ $(1 - a)$ where $1 \text{ m} < \tilde{h} < 5$ m. For small a, $G = 1.21 + 4.6a$ (the error in $G - 1.0$ is less than or equal to 5% when compared to results obtained from a numerical integration of (38)). Now a is approximately the areal percentage of young ice. From the discussion by *Maykut* [1982], a is uncertain but is probably in the range 5 to 10%, so that $1.44 < G < 1.67$. However, from submarine measurements in the central Arctic, [*Bourke* (1987] indicates a much higher value of about 20% (with some seasonal variability); our simple formula yields a value of $G = 1.9$, whereas a numerical integration of (39) using Bourke's measured ice distribution yields 2.1.

We again ran the model for div $\mathbf{V} = 4 \times 10^{-9}$ s^{-1}, but this time $G = 1.5$, instead of unity, which effectively means that we increase the conductivity k by 50%. (For want of a more enlightened strategy we apply this increase to both the ice and snow values, k_I and k_s.) This calculation yielded a value $\langle Ah_I \rangle = 2.49$. Finally, we specified $h_s = 0.10$ m and obtained $\langle Ah_I \rangle = 2.93$. (The result is quite similar to Figure 15 except that Ah_I is higher, A has a minimum value of 0.91, and the amplitude of the curve in Figure 15*c* is about 30% larger. The T and S contours are nearly identical.)

8. Summary and Conclusions

The main goal of this paper was to produce an ice model which can be matched and is otherwise compatible with a turbulence closure, mixed layer model and which, subsequently, can be wedded to a three-dimensional model within which the mixed layer model is embedded. This goal, we believe, has been reached.

Some specific findings are as follows: Ocean coupling does introduce considerable variability in the ocean surface heat flux. A net result is to lower the annual and area-averaged ice thickness, but only by 0 to 15%, depending on the value of the molecular sublayer constant b. (We obtained the decoupled ice result by interpolating Figure 8*a* for a mean ocean heat flux of 0.33 W m^{-2}, generated by the coupled model.) It should be noted that the mean oceanic surface heat flux had been thought to be about 2 W m^{-2}, although the number has been challenged. However, the data (and the model) yield the value 0.33 W m^{-2} for a pycnocline mixing coefficient of 0.2 cm^2 s^{-1}, which is probably an overly large estimate for the central Arctic; thus this study is supportive of a oceanic heat flux of 0.3 W m^{-2} or less. An estimate of upwelling heat flux using div $\mathbf{V} = 4 \times 10^{-9}$ s^{-1} and some Ekman layer velocity structure information does not seem to alter this conclusion.

The effect of allowing for melt pools increases the annual mean ice thickness through the use of the parameter $h_{sw} > 0$. The same parameter can roughly account for the penetration of shortwave penetration into the ice.

The ice model contains the empirical lead parameters Φ_M and Φ_F. Results, such as the annual mean ice thickness, are quite insensitive to Φ_M so long as $\Phi_F \geq 2$, which does include the physically probable range. On the other hand, annual mean thickness is sensitive to Φ_M in the physically reasonable range $1.0 > \Phi_M > 0.5$.

The parameter b determines the level of resistance for heat and salinity flux in the molecular layer between the ice and the oceanic mixed layer. We consider the range $0 \leq b \leq 3.0$ (for $b = 0$, there is no molecular layer). In the marginal ice zone the effect of b is pronounced [*McPhee et al.*, 1987; *Steele et al.*, 1989] in that increasing b significantly decreases melt rate at the ice edge. In these central Arctic simulations the ice thickness response to b is not large. However, $b > 0$ does produce the observed seasonal temperature signal, and frazil ice is created. The calculated frazil ice production is apparently too large. *Tucker et al.* [1987] report that the percentage of frazil ice to congelate ice in forty floes emerging through the Fram Straits is about 20%, as compared to our calculated 31 to 37%. Of course, we have converted all supercooled water to equilibrium, whereas the water column must retain a degree of supercooling to provide the driving potential for frazil ice freezing. More detailed research and modeling is required on this aspect of the overall frazil ice problem.

We have surveyed the effect of div $\mathbf{V}$ for the coupled ice model and found it to be a major factor. First, it can be an

important part of the ice budget. Second it can produce summertime concentrations less than unity. In the coupled ocean-ice model we first fixed div $\mathbf{V} = 2 \times 10^{-9}$ s^{-1}. However, observations indicate actual values of 4×10^{-9} s^{-1} or greater. Using this value, the model yielded ice thicknesses which were far below those observed. This led to the invention of an empirical factor G to account for the fact that the average thickness h_I, which correctly describes ice volume, is not the thickness that should be used in the ice conduction equation. Although its value is uncertain, we feel that G is a factor required by the class of ice models whose independent variables are A and h_I and which do not deal directly with the distribution function $g(\tilde{h})$.

In general, we believe that the ice model, the ocean mixed layer model, and the means of matching the models described in this paper provide a good basis for three-dimensional simulations of the polar oceans and the marginal ice zones.

Appendix A: Atmospheric Bulk Formulas

Equations for heat fluxes are provided here for convenience. They are not used in this paper, except to provide open water corrections to Table 2, but they are used in the companion paper by *Kantha and Mellor* [this issue], and it is expected that they will be used in most future applications of the model.

The shortwave radiation SW is a function of astronomical parameters and is given by [*Parkinson and Washington*, 1979]

$$SW = \frac{S_c \cos^2 \theta_z (1 - 0.6\, C_l^3)}{10^{-5} (\cos \theta_z + 2.7) e_A + 1.085 \cos \theta_z + 0.10} \tag{A1}$$

where $S_c = 1353$ W m^{-2} is the solar constant, C_l is the fractional cloud cover, and θ_z is the solar zenith angle. The atmospheric vapor pressure e_A (in Pascals) is related to the specific humidity q_A and the atmospheric pressure p by

$$\frac{e_A}{p} = \frac{q_A}{0.622 + 0.378 q_A} \tag{A2}$$

The cosine of the zenith angle $\cos \theta_z$ is given by

$$\cos \theta_z = \sin \phi \sin \delta + \cos \phi \cos \delta \cos \psi \tag{A3a}$$

where ϕ is the latitude; δ, the declination, and ψ, the hour angle, are given approximately by

$$\delta = 23.44° \cos [360°(172 - D_y)/365] \tag{A3b}$$

$$\psi = 15°(12 - T_H) \tag{A3c}$$

where D_y is the day of the year and T_H is the solar time in hours.

The longwave flux LW is taken as (following *Maykut and Perovich* [1987])

$$LW = \sigma (T_A + 273)^4 (0.7855 + 0.2232\, C_l^{2.75}) \tag{A4}$$

where T_A is the temperature in degrees Celsius of the surface layer of air.

The direct atmospheric stresses imposed on ice and open water are given by

$$(\tau_{AIx}, \tau_{AIy}) = C_{DAI} \rho_a |\mathbf{U}_{10}| (U_{10}, V_{10}) \tag{A5}$$

$$(\tau_{AOx}, \tau_{AOy}) = C_{DAO} \rho_a |\mathbf{U}_{10}| (U_{10}, V_{10}) \tag{A6}$$

where $\mathbf{U}_{10} = (U_{10}, V_{10})$ is the 10-m anemometer wind vector. The sensible and latent heat fluxes between the ice and the atmosphere are

$$Q_{SI} = \rho_a C_{pa} C_{HAI} |\mathbf{U}_{10}| (T_3 - T_A) \tag{A7}$$

$$Q_{LI} = \rho_a L_s C_{HAI} |\mathbf{U}_{10}| (q_3 - q_A) \tag{A8}$$

L_s is the latent of sublimation and q_3 is the saturation specific humidity based on T_3 [*Gill*, 1982, p. 606]. The sensible and latent heat fluxes between the atmosphere and open water are

$$Q_{SO} = \rho_a C_{pa} C_{HO} |\mathbf{U}_{10}| (T_o - T_A) \tag{A9}$$

$$Q_{LO} = \rho_a L_v C_{HO} |\mathbf{U}_{10}| (q_0 - q_A) \tag{A10}$$

q_0 is the saturated specific humidity based on the open ocean surface temperature T_0 [*Gill*, 1982, p. 606]. L_v is the latent heat of vaporization. The bulk coefficients used in this paper are

$$C_{DAI} = 3.0 \times 10^{-3} \qquad C_{DAO} = 1.5 \times 10^{-3}$$

$$C_{HAI} = 1.5 \times 10^{-3} \qquad C_{HAO} = 1.5 \times 10^{-3}$$

Appendix B: Some Computational Details

During the course of numerical integration, let T_{3p} be the value of the ice surface temperature at the previous time step. Expand the current value according to $T_3^4 = T_{3p}^4 + 4T_{3p}^3 (T_3 - T_{3p})$. Then the combination of (8), (9*a*), and (9*b*) can be written $T_3 = T_{3p} - [\sigma T_{3p}^4 + Q_{AI} - Q_{I2}][4\sigma T_{3p}^3 + (h_I/(2k_I) + h_s/k_s)]^{-1}$; this is the equation used to update the ice or snow surface temperature so long as T_3 is less than the freezing temperature.

Equations (16*a*), (17), (20), (21), and (23*b*) may be combined to yield

$$W_O = -\frac{b}{2} - \frac{1}{2}[b^2 - 4c]^{1/2} \tag{B1}$$

where, if we set $\tilde{C}_{Tz} = \rho_o C_{po} C_{Tz}$, then

$$b = -C_{Sz} + \frac{\tilde{C}_{Tz}}{L_o}(T - mS_I) - \frac{1}{L_o}[(1 - A)Q_{AO} + AQ_{IO}]$$

$$c = -\frac{\tilde{C}_{Tz} C_{Sz}}{L_o}(T - mS) + \frac{C_{Sz}}{L_o}[(1 - A)Q_{AO} + AQ_{IO}]$$

$$- m \frac{\tilde{C}_{Tz}}{L_o}[(1 - A)S_0(\tilde{P} - \tilde{E}) + A(S_o - S_I)W_{RO}]$$

Thus W_O is obtained from (B1) if $A = 0$, $W_O = 0$. (Note again that T and S refer to near-surface values determined by solutions to the ocean model.) Then F_T and T_0 are obtained from (16*a*) and (17) and F_S and S_0 are obtained from (20) and (21). Finally, W_{IO} and W_{AO} are obtained from (15*a*) and (15*b*) for use in equations (3) and (4).

While equation (B1) has been useful to the development of the model and is useful in explicitly relating W_O to relevant variables, we have finally found it possible and numerically simpler to use the original equations in a quasi-iterative sense where, using W_O and W_{RO} from the previous time level, (20) and (21) are solved for S_0; then (23*b*) yields T_0; (17) yields F_T, and finally, W_{IO} and W_{AO} are obtained from (15*a*) and (15*b*).

Acknowledgments. This research was supported by the Arctic Program of the Office of Naval Research under contract N00014-84-0640. Computer support was provided by NOAA's Geophysical Fluid Dynamics Laboratory. We wish to thank AOS Program secretaries for typing the manuscript and the GFDL drafting department for figure preparation.

REFERENCES

Bauer, J., and S. Martin, A model of grease ice growth in small leads, *J. Geophys. Res.*, *88*, 2917–2925, 1983.

Blumberg, A. F., and G. L. Mellor, Diagnostic and prognostic numerical circulation studies of the South Atlantic Bight, *J. Geophys. Res.*, *88*, 4579–4592, 1983.

Blumberg, A. F., and G. L. Mellor, A description of a three-dimensional coastal ocean circulation model, in *Three-Dimensional Coastal Ocean Models, Coastal and Estuarine Sci. Ser.*, vol. 4, edited by N. Heaps, pp. 1–16, AGU, Washington, D. C., 1987.

Bourke, R. H., and R. P. Garrett, Sea ice thickness in the Arctic Ocean, *Cold Reg. Sci. Technol.*, *13*, 259–280, 1987.

Colony, R., and A. S. Thorndike, An estimate of the mean field of Arctic sea ice motion, *J. Geophys. Res.*, *89*, 10,623–10,629, 1984.

Fletcher, J. O., The heat budget of the Arctic basin and its relation to climate, *R-444-PR*, The Rand Corp., Santa Monica, Calif., 1965.

Fujino, K., E. L. Lewis, and R. G. Perkins, The freezing point of seawater at pressures up to 100 bars, *J. Geophys. Res.*, *79*, 1792–1797, 1974.

Gill, A. E., *Atmosphere-Ocean Dynamics*, *Int. Geophys. Ser.*, vol 30, 662 pp., Academic, San Diego, Calif., 1982.

Gorshkov, S. G. (Ed.), *World Ocean Atlas, Arctic Ocean*, *3*, 189 pp., Pergamon, New York, 1983.

Hibler, W. D., III, A dynamic thermodynamic sea ice model, *J. Phys. Oceanogr.*, *9*, 815–846, 1979.

Hibler, W. D., III, Modeling a variable thickness ice cover, *Mon. Weather Rev.*, *108*, 1943–1973, 1980.

Hibler, W. D., III, and K. Bryan, A diagnostic ice-ocean model, *J. Phys. Oceanogr.*, *17*, 987–1015, 1987.

Ikeda, M., A mixed layer beneath melting sea ice in the marginal ice zone using a one-dimensional turbulent closure model, *J. Geophys. Res.*, *91*, 5054–5060, 1986.

Josberger, E. G., Sea ice melting in the marginal ice zone, *J. Geophys. Res.*, *88*, 2841–2844, 1983.

Kantha, L. H., and G. L. Mellor, A two-dimensional coupled ice-ocean model of the Bering Sea marginal ice zone, *J. Geophys. Res.*, this issue.

Klein, P., A simulation of the effects of air-sea transfer variability on the structure of the marine upper layers, *J. Phys. Oceanogr.*, *10*, 1824–1841, 1980.

Kolmogorov, A. N., The local structure of turbulence in incompressible viscous fluid for very large Reynolds number (in Russian), *Dokl. Akad. Nauk SSSR*, *30*, 299–303, 1941.

Lemke, P., A coupled one-dimensional sea ice-ocean model, *J. Geophys. Res.*, *92*, 13,164–13,172, 1987.

Levitus, S., *Climatological Atlas of the World Ocean*, *NOAA Prof. Pap.*, *13*, 173 pp., U.S. Goverment Printing Office, Washington, D. C., 1982.

Martin, P. J., Simulation of the mixed layer at OWS November and Papa with several models, *J. Geophys. Res.*, *90*, 903–916, 1985.

Maykut, G. A., Large-scale heat exchange and ice production in the Central Arctic, *J. Geophys. Res.*, *87*, 7971–7984, 1982.

Maykut, G. A., and D. K. Perovich, The role of shortwave radiation in the summer decay of a sea ice cover, *J. Geophys. Res.*, *92*, 7032–7044, 1987.

Maykut, G. A., and N. Untersteiner, Some results from a time dependent thermodynamic model of sea ice, *J. Geophys. Res.*, *76*, 1550–1575, 1971.

McPhee, M. G., G. A. Maykut, and J. H. Morrison, Dynamics and thermodynamics of the ice/upper ocean systems in the marginal ice zone of the Greenland Sea, *J. Geophys. Res.*, *92*, 7017–7031, 1987.

Mellor, G. L., Analytic prediction of the properties of stratified planetary surface layers, *J. Atmos. Sci.*, *30*, 1061–1069, 1973.

Mellor, G. L., and T. Yamada, A hierarchy of turbulence closure models for planetary boundary layers, *J. Atmos. Sci.*, *31*, 1791–1806, 1974.

Mellor, G. L., and T. Yamada, Development of a turbulence closure model for geophysical fluid problems, *Rev. Geophys.*, *20*, 851–875, 1982.

Mellor, G. L., M. G. McPhee, and M. Steele, Ice-seawater turbulent boundary layer interaction with melting or freezing, *J. Phys. Oceanogr.*, *16*, 1829–1846, 1986.

Morrison, J., and J. D. Smith, Seasonal variation in the upper Arctic ocean as observed at T-3, *Geophys. Res. Lett.*, *8*, 753–756, 1981.

Nikiferov, E. G., Variations in ice cover compaction due to its dynamics, in *Problemy Arktiki*, vol. 2, Morskoi Transport Press, Leningrad, USSR, 1957.

Oey, L.-Y., G. L. Mellor, and R. I. Hires, A three-dimensional simulation of the Hudson-Raritan estuary, I, Description of the model and model simulations, *J. Phys. Oceanogr.*, *15*, 1676–1692, 1985*a*.

Oey, L.-Y., G. L. Mellor, and R. I. Hires, A three-dimensional simulation of the Hudson-Raritan estuary, II, Comparison with observation, *J. Phys. Oceanogr.*, *15*, 1693–1709, 1985*b*.

Oey, L.-Y., G. L. Mellor, and R. I. Hires, A three-dimensional simulation of the Hudson-Raritan estuary, III, Salt flux analyses, *J. Phys. Oceanogr.*, *15*, 1711–1720, 1985*c*.

Owen, P. R., and W. R. Thompson, Heat transfer across rough surfaces, *J. Fluid Mech.*, *15*, 321–334, 1963.

Parkinson, C. L., and W. M. Washington, A large-scale numerical model of sea ice, *J. Geophys. Res.*, *84*, 311–337, 1979.

Rotta, J. C., Statistische theorie nichthomogener turbulenz, 1, *Z. Phys.*, *129*, 547–572, 1951*a*.

Rotta, J. C., Statistische theorie nichthomogener turbulenz, 2, *Z. Phys.*, *131*, 51–77, 1951*b*.

Schlichting, H., *Boundary Layer Theory*, 7th ed., 747 pp., McGraw-Hill, New York, 1978.

Semtner, A. J., Jr., A model for the thermodynamic growth of sea ice in numerical investigation of climate, *J. Phys. Oceanogr.*, *6*, 379–389, 1976*a*.

Semtner, A. J., Jr., Numerical simulation of the Arctic Ocean circulation, *J. Phys. Oceanogr.*, *6*, 409–425, 1976*b*.

Semtner, A. J., Jr., A numerical study of sea ice and ocean circulation in the Arctic, *J. Phys. Oceanogr.*, *17*, 1077–1099, 1987.

Simpson, J. J., and T. D. Dickey, The relationship between irradiance and upper ocean structure, *J. Phys. Oceanogr.*, *11*, 309–323, 1981.

Steele, M., G. L. Mellor, and M. G. McPhee, The role of the molecular sublayer in the melting or freezing of sea ice, *J. Phys. Oceanogr.*, *19*, 139–147, 1989.

Taylor, P. A., Comments and further analysis on effective roughness lengths for use in numerical three-dimensional models, *Boundary Layer Meteorol.*, *39*, 403–418, 1987.

Thorndyke, A. S., D. A. Rothrock, G. A. Maykut, and R. Colony, The thickness distribution of sea ice, *J. Geophys. Res.*, *80*, 4501–4513, 1975.

Tucker, W. B., A. J. Gow, and W. F. Weeks, Physical properties of summer sea ice in the Fram Strait, *J. Geophys. Res.*, *92*, 6787–6803, 1987.

Untersteiner, N., On the mass and heat budget of arctic sea ice, *Arch. Meteorol. Geophys. Bioklimatol.*, *12*, 151–182, 1961.

Vinje, T., and O. Finnekasa, The ice transport through the Fram Strait, *Skr. Nor. Polarinst.*, *186*, 39 pp., 1986.

White, W., and R. Bernstein, Large-scale vertical eddy diffusion in the main pycnocline of the central North Pacific, *J. Phys. Oceanogr.*, *11*, 434–441, 1981.

Yaglom, A. M., and B. A. Kader, Heat and mass transfer between a rough wall and turbulent fluid at high Reynolds and Peclet numbers, *J. Fluid Mech.*, *62*, 601–623, 1974.

L. Kantha, Institute of Naval Oceanography, Stennis Space Center, MS 39529.

G. L. Mellor, Atmospheric and Oceanic Sciences Program, Princeton University, James Forrestal Campus, P. O. Box 308, Princeton, NJ 08542.

(Received June 6, 1988;
revised January 18, 1989;
accepted October 27, 1988.)